

---

# INITIALIZATION SCHEMES FOR KOLMOGOROV–ARNOLD NETWORKS: AN EMPIRICAL STUDY

---

**Spyros Rigas\***

Department of Digital Industry Technologies  
National and Kapodistrian University of Athens  
344 00 Psachna, Greece  
[sprigas@uoa.gr](mailto:sprigas@uoa.gr)

**Dhruv Verma**

Applied and Computational Mathematics  
California Institute of Technology  
Pasadena, CA 91125, United States of America  
[dverma@caltech.edu](mailto:dverma@caltech.edu)

**Georgios Alexandridis**

Department of Digital Industry Technologies  
National and Kapodistrian University of Athens  
344 00 Psachna, Greece  
[gealexandri@uoa.gr](mailto:gealexandri@uoa.gr)

**Xixuan Wang**

Applied and Computational Mathematics  
California Institute of Technology  
Pasadena, CA 91125, United States of America  
[roywang@caltech.edu](mailto:roywang@caltech.edu)

## ABSTRACT

Kolmogorov–Arnold Networks (KANs) are a recently introduced neural architecture that replace fixed nonlinearities with trainable activation functions, offering enhanced flexibility and interpretability. While KANs have been applied successfully across scientific and machine learning tasks, their initialization strategies remain largely unexplored. In this work, we study initialization schemes for spline-based KANs, proposing two theory-driven approaches inspired by LeCun and Glorot, as well as an empirical power-law family with tunable exponents. Our evaluation combines large-scale grid searches on function fitting and forward PDE benchmarks, an analysis of training dynamics through the lens of the Neural Tangent Kernel, and evaluations on a subset of the Feynman dataset. Our findings indicate that the Glorot-inspired initialization significantly outperforms the baseline in parameter-rich models, while power-law initialization achieves the strongest performance overall, both across tasks and for architectures of varying size. All code and data accompanying this manuscript are publicly available at [https://github.com/srigas/KAN\\_Initialization\\_Schemes](https://github.com/srigas/KAN_Initialization_Schemes).

## 1 Introduction

Kolmogorov–Arnold Networks (KANs) [Liu et al., 2025] have recently emerged as an alternative backbone architecture to Multilayer Perceptrons (MLPs), drawing inspiration from the Kolmogorov–Arnold representation theorem [Kolmogorov, 1957] in a manner analogous to how the learning of MLPs relies on universal approximation theorems. Unlike MLPs, which use fixed nonlinear activation functions and trainable synaptic weights, KANs comprise grid-dependent trainable activation functions. This provides them with flexibility in modeling complex nonlinear relationships, while requiring fewer and smaller layers. Since their introduction, KANs have found numerous applications, often surpassing the performance of their MLP-based counterparts [Yu et al., 2024, Poeta et al., 2024]. There have been many notable results in scientific problem-solving domains, including function fitting and symbolic regression [Liu et al., 2024, Shukla et al., 2024], partial differential equations (PDEs) [Shukla et al., 2024, Rigas et al., 2024, Wang et al., 2025a] and operator learning [Abueidda et al., 2025, Shukla et al., 2024], among other applications [Howard et al., 2024, Kundu et al., 2024, Kashefi, 2025].

Beyond these benchmarks, there has also been significant progress in the theoretical understanding of KANs [Zhang and Zhou, 2025, Alter et al., 2025, Wang et al., 2025b]. However, one important theoretical and practical aspect that remains understudied pertains to their initialization strategies. Current literature mainly relies on the standard initialization

---

\*Corresponding author.

---

method proposed in the introductory KAN paper [Liu et al., 2025], or explores alternative KAN variants such as Chebyshev-based formulations [Rigas et al., 2025]. This highlights a clear gap and motivates an investigation into more effective initialization approaches for the standard spline-based architecture. Effective initialization is crucial, as a good “initial guess” for the network weights can significantly accelerate training [Mishkin and Matas, 2016, Skorski et al., 2021] and prevent early saturation of hidden layers [Glorot and Bengio, 2010]. However, despite extensive research into initialization methods for MLP-based architectures, these results cannot be directly applied to KANs. Furthermore, even within MLP-based architectures, initialization methods often require separate consideration depending on the specific architecture design [Huang et al., 2020], activation function [He et al., 2015], or even on a complete case-by-case basis [Skorski et al., 2021].

In response to this research gap, this work explores initialization strategies for the standard, spline-based KAN architecture. Drawing parallels with MLPs, we propose variance-preserving schemes inspired by LeCun [LeCun et al., 1998] and Glorot [Glorot and Bengio, 2010] initializations, including a variant that employs batch-normalized [Ioffe and Szegedy, 2015] spline basis functions. In addition, recognizing that theoretical frameworks may not always align with empirical performance [Mishkin and Matas, 2016], we further propose an empirical family of power-law initializations with tunable exponents. To evaluate these approaches, we conduct extensive grid searches on function fitting tasks and forward PDE problems. Beyond final error metrics, we further compare the different initialization schemes through an analysis of training dynamics, examining the evolution of loss curves and the Neural Tangent Kernel (NTK) spectrum Jacot et al. [2018], Wang et al. [2022] for representative architectures. Finally, we evaluate said architectures on a subset of the Feynman dataset [Udrescu and Tegmark, 2020], which, although widely used for symbolic regression, is formulated here as a function fitting benchmark as in Liu et al. [2025].

## 2 Background

### 2.1 Kolmogorov–Arnold Networks

Within the standard formalism, the output,  $\mathbf{y} \in \mathbb{R}^{n_{\text{out}}}$ , of a KAN layer is related to its input,  $\mathbf{x} \in \mathbb{R}^{n_{\text{in}}}$ , via:

$$y_j = \sum_{i=1}^{n_{\text{in}}} \left( r_{ji} R(x_i) + c_{ji} \sum_{m=1}^{G+k} b_{jim} B_m(x_i) \right), \quad j = 1, \dots, n_{\text{out}}, \quad (1)$$

where  $r_{ji}$ ,  $c_{ji}$  and  $b_{jim}$  are the layer’s trainable parameters,  $R(x)$  corresponds to a residual function, typically chosen as the SiLU, i.e.,  $R(x) = x(1 + e^{-x})^{-1}$ , and  $B_m(x)$  denotes a univariate spline basis function of order  $k$ , defined on a grid with  $G$  intervals. For each of the layer’s trainable parameters, the original KAN formulation initializes the scaling weights as  $c_{ji} = 1$ , the residual weights  $r_{ji}$  using Glorot initialization [Glorot and Bengio, 2010], and the basis weights  $b_{jim}$  from a normal distribution with zero mean and small standard deviation, typically set to  $\sigma = 0.1$ . We will henceforth refer to this configuration as the “baseline initialization”.

### 2.2 Related Work

In the existing KAN literature, initialization strategies have only been explored in certain KAN variants (see, e.g., Guilhoto and Perdikaris [2025]), while the standard spline-based architecture has not yet received dedicated attention in this regard. A natural starting point for studying initialization is to follow the historical developments in MLP-based architectures, beginning with variance-preserving schemes such as those proposed by LeCun [LeCun et al., 1998] and Glorot [Glorot and Bengio, 2010], which stabilize activation variance across layers and mitigate progressive vanishing or explosion. Alternatively, architectural modifications such as batch normalization [Ioffe and Szegedy, 2015] have been introduced to maintain stable activation distributions and reduce sensitivity to initialization. Within the KAN family, Glorot-inspired initialization has been applied successfully to Chebyshev-based variants [Rigas et al., 2025], though this setting differs substantially from the spline-based case studied here, since it removes the residual term of Eq. (1) and employs a completely different basis function. Consequently, it remains unclear whether such strategies directly transfer to the standard KAN formulation, motivating the investigation presented in this work. To the best of our knowledge, the present work provides the first systematic study of initialization strategies for spline-based KANs.

### 3 Methodology

#### 3.1 Proposed Initializations

Since the three weight types in a KAN layer are independent, we may initialize the scaling weights  $c_{ji}$  to 1 and focus exclusively on the initialization of the residual weights  $r_{ji}$  and basis weights  $b_{jim}$ . We assume that these weights are drawn from zero-mean distributions with standard deviations  $\sigma_r$  and  $\sigma_b$ , respectively. To determine suitable values for  $\sigma_r$  and  $\sigma_b$ , we follow the principle of variance preservation proposed by LeCun [LeCun et al., 1998], which stipulates that the variance of the outputs of each layer should match that of its inputs, thereby avoiding amplification or attenuation of the signal across layers. Assuming statistical independence among terms and an equal contribution to the variance from each of the  $(G + k + 1)$  terms in the summand of Eq. (1), we derive the following expressions for the standard deviations<sup>2</sup>:

$$\sigma_r = \sqrt{\frac{\text{Var}(x_i)}{n_{\text{in}}(G + k + 1) \mu_R^{(0)}}}, \quad \sigma_b = \sqrt{\frac{\text{Var}(x_i)}{n_{\text{in}}(G + k + 1) \mu_B^{(0)}}}, \quad (2)$$

where

$$\mu_R^{(0)} = \mathbb{E} [R(x_i)^2], \quad \mu_B^{(0)} = \mathbb{E} [B_m(x_i)^2], \quad (3)$$

with  $\mu_B^{(0)}$  denoting the expectation over both the input distribution and all spline basis indices,  $m$ , and  $\mu_R^{(0)}$  denoting the expectation over the input distribution alone.

If we further assume that each component of  $\mathbf{x}$  is drawn from a given distribution (e.g., the uniform distribution  $\mathcal{U}(-1, 1)$ , as is often the case in tasks like function fitting or PDE solving), then all statistical quantities in Eq. (2) can be evaluated directly, except for  $\mu_B^{(0)}$ . Due to the dependence of the spline-basis functions on the underlying grid, no general analytic expression exists for  $\sigma_b$ . This leads to two practical alternatives: one may either estimate  $\mu_B^{(0)}$  numerically by sampling a large number of input points from the assumed distribution at initialization, or set the expectation value to unity by modifying the architecture of the KAN layer to use batch-normalized spline basis functions, defined as

$$\tilde{B}_m(x_i) = \frac{B_m(x_i) - \mathbb{E}[B_m(x_i)]}{\sqrt{\mu_B^{(0)} - \mathbb{E}^2[B_m(x_i)]}}, \quad (4)$$

where the expectation values are computed over the current batch during each forward pass. We will refer to the former alternative as ‘‘LeCun–numerical’’ initialization, while the latter is referred to as ‘‘LeCun–normalized’’ initialization.

While these LeCun-inspired schemes focus on preserving the variance of forward activations, they do not explicitly account for the propagation of gradients. To address this, we also consider a Glorot-inspired initialization, which aims to balance forward- and backward-pass variance by maintaining stable variance for both activations and gradients across layers. Under the same assumptions as before, we derive the following expressions for the standard deviations<sup>3</sup>:

$$\sigma_r = \sqrt{\frac{1}{G + k + 1} \cdot \frac{2}{n_{\text{in}} \mu_R^{(0)} + n_{\text{out}} \mu_R^{(1)}}}, \quad \sigma_b = \sqrt{\frac{1}{G + k + 1} \cdot \frac{2}{n_{\text{in}} \mu_B^{(0)} + n_{\text{out}} \mu_B^{(1)}}}, \quad (5)$$

where

$$\mu_R^{(1)} = \mathbb{E} [R'(x_i)^2], \quad \mu_B^{(1)} = \mathbb{E} [B'_m(x_i)^2], \quad (6)$$

with the expectations defined analogously to  $\mu_R^{(0)}$  and  $\mu_B^{(0)}$  in Eq. (3). In practice,  $\mu_B^{(1)}$  can be computed using automatic differentiation of the spline basis functions, together with the numerical sampling strategy discussed for the LeCun–numerical case, while  $\mu_R^{(1)}$  can be evaluated analytically for standard choices of  $R(x)$  such as the SiLU.

<sup>2</sup>See Appendix A for detailed derivations.

<sup>3</sup>See Appendix B for detailed derivations.

In addition to these theory-driven initialization strategies, we also investigate an empirical approach based on a power-law scaling of the KAN layer’s architectural parameters. Specifically, we initialize the weights such that their standard deviations follow the form

$$\sigma_r = \left( \frac{1}{n_{\text{in}} (G + k + 1)} \right)^\alpha, \quad \sigma_b = \left( \frac{1}{n_{\text{in}} (G + k + 1)} \right)^\beta, \quad (7)$$

where  $\alpha$  and  $\beta$  are tunable exponents selected from the set  $\{0.0, 0.25, \dots, 1.75, 2.0\}$ . The motivation behind this empirical scheme is to perform a grid search over  $(\alpha, \beta)$  configurations in order to identify trends or specific exponent pairs that consistently improve training speed and convergence, potentially revealing an effective heuristic for initializing KANs.

### 3.2 Experimental Setup

We evaluate initialization strategies on two benchmark families: function fitting tasks and forward PDE problems. For function fitting, we use five two-dimensional target functions and train for 2,000 epochs, while for PDEs we consider the Allen–Cahn equation, Burgers’ equation, and the two-dimensional Helmholtz equation, using KANs trained for 5,000 epochs within the Physics-Informed Machine Learning (PIML) framework [Raissi et al., 2019]. Across both benchmarks, performance is measured using the final training loss and the relative  $L^2$  error with respect to the reference solution. For the purposes of the initial grid search, we test architectures with 1–4 hidden layers, widths equal to  $2^i$  for  $i = 1, \dots, 6$ , and grid sizes  $G \in \{5, 10, 20, 40\}$  for function fitting, while for PDEs we restrict to  $G \in \{5, 10, 20\}$ . All experiments presented herein are repeated with five random seeds, except in the power-law grid search where we use three seeds to reduce computational cost, and we report the median outcome across runs. Further implementation details, including the explicit formulas of the target functions and the PDE setups, are provided in Appendix C. All experiments are implemented in JAX [Bradbury et al., 2018], with KANs trained using the jaxKAN framework [Rigas and Papachristou, 2025]. Training is performed on a single NVIDIA GeForce RTX 4090 GPU.

## 4 Experiments & Discussion

### 4.1 Grid-Search Results

The grid search over  $(\alpha, \beta)$  configurations and the architectural variations described in Section 3.2 resulted in 126,240 trained KAN model instances for function fitting. After aggregating the repeated runs by their median outcome, this number reduces to 40,800 representative results. From these, we retain only the best-performing  $(\alpha, \beta)$  configuration per setting, yielding 2,400 final entries. Table 1 reports, for each target function and initialization scheme, the percentage of runs that outperform the baseline initialization described in Section 2.1. Results are compared with respect to final training loss and relative  $L^2$  error, and we additionally report the percentage of runs where both metrics improve simultaneously.

Table 1: Percentage of runs that outperform the baseline initialization on function fitting benchmarks. Columns correspond to target functions, while rows correspond to initialization schemes and evaluation metrics. Best results per function are shown in bold.

Initialization	Metric	$f_1(x, y)$	$f_2(x, y)$	$f_3(x, y)$	$f_4(x, y)$	$f_5(x, y)$
LeCun–numerical	Loss	18.75%	14.58%	12.50%	25.00%	26.04%
	$L^2$	6.25%	4.17%	5.21%	14.58%	2.08%
	Both	1.04%	0.00%	0.00%	8.33%	0.00%
LeCun–normalized	Loss	19.79%	28.13%	19.79%	41.67%	31.25%
	$L^2$	11.46%	9.38%	11.46%	26.04%	6.25%
	Both	2.08%	5.21%	5.21%	16.67%	1.04%
Glorot	Loss	78.13%	76.04%	78.13%	63.54%	72.92%
	$L^2$	78.13%	75.00%	78.13%	64.58%	72.92%
	Both	78.13%	75.00%	78.13%	60.41%	64.59%
Power-Law	Loss	<b>100.00%</b>	<b>100.00%</b>	<b>100.00%</b>	<b>100.00%</b>	<b>98.96%</b>
	$L^2$	<b>100.00%</b>	<b>100.00%</b>	<b>100.00%</b>	<b>94.79%</b>	<b>96.88%</b>
	Both	<b>100.00%</b>	<b>100.00%</b>	<b>100.00%</b>	<b>94.79%</b>	<b>95.83%</b>

We observe that, in nearly all cases, a suitable power-law initialization outperforms the baseline scheme across both metrics. In contrast, the LeCun-inspired strategies yield more mixed outcomes: while they rarely outperform the baseline on small architectures, the normalized variant in particular becomes more effective as depth, width and grid size increase, in some cases providing improvements of over two orders of magnitude. The Glorot-inspired initialization performs consistently better than both the baseline and the LeCun-based schemes, with success rates above 60%–75% across all functions, though it still falls short of the power-law family. Importantly, the more favorable power-law configurations tend to correspond to relatively small values of  $\alpha$  (e.g., near 0.25) combined with larger  $\beta$  values (i.e.,  $\geq 1.5$ ), leading to substantially lower final losses. The complete grid-search results, where these trends can be directly observed, are provided in Appendix D and the supplementary material.

For the PDE benchmarks, the same procedure produced 56,882 trained models, which reduced to 18,360 representative results after aggregation and 1,080 final entries after selecting the best  $(\alpha, \beta)$  per setting. Table 2 summarizes the outcomes in terms of final training loss, relative  $L^2$  error, and their joint improvement over the baseline initialization. The power-law initialization dominates in nearly all cases when judged by final loss and also achieves strong results when both metrics are considered simultaneously, although the improvements are less widespread than in the function fitting benchmarks. This is expected, since favorable initialization for function fitting does not directly transfer to PDE problems, where derivatives are involved and introduce additional complexity [Wang et al., 2024]. The Glorot-inspired scheme provides a competitive alternative, with success rates of roughly 50–75% depending on the PDE, while both LeCun-based variants prove largely ineffective, with the normalized version in particular failing to improve over the baseline at all. Interestingly, this stands in contrast to the function fitting benchmarks, where the normalized variant outperformed the numerical one, again proving that PDE problems introduce qualitatively different dynamics in how initialization interacts with training. Finally, while the specific  $(\alpha, \beta)$  configurations that perform best in PDEs differ from those in function fitting, the general trend persists: smaller values of  $\alpha$  and larger values of  $\beta$  are favored. The complete grid-search results supporting these observations are provided in Appendix D and the supplementary material.

Table 2: Percentage of runs that outperform the baseline initialization on forward PDE benchmarks. Columns correspond to the three PDEs considered, while rows correspond to initialization schemes and evaluation metrics. Best results per PDE are shown in bold.

Initialization	Metric	Allen–Cahn	Burgers	Helmholtz
LeCun–numerical	Loss	11.11%	11.11%	8.33%
	$L^2$	16.67%	22.22%	15.28%
	Both	8.33%	6.94%	2.78%
LeCun–normalized	Loss	2.78%	0.00%	0.00%
	$L^2$	0.00%	0.00%	0.00%
	Both	0.00%	0.00%	0.00%
Glorot	Loss	55.56%	50.00%	76.39%
	$L^2$	51.39%	54.17%	72.22%
	Both	41.67%	36.11%	62.50%
Power-Law	Loss	<b>98.61%</b>	<b>100.00%</b>	<b>98.61%</b>
	$L^2$	<b>94.44%</b>	<b>73.61%</b>	<b>87.50%</b>
	Both	<b>94.44%</b>	<b>73.61%</b>	<b>87.50%</b>

## 4.2 Training Dynamics Analysis

The grid-search experiments established that Glorot- and power-law-based schemes provide strong alternatives to the baseline initialization, with the latter yielding the most consistent improvements overall. To better understand the mechanisms behind these trends, we next examine training dynamics in greater detail, focusing only on the baseline, Glorot-inspired, and power-law schemes. We begin with the function fitting benchmarks: Figure 1 shows the evolution of the training loss for two representative settings, a “small” architecture ( $G = 5$ , two hidden layers with 8 neurons each) and a “large” architecture ( $G = 20$ , three hidden layers with 32 neurons each). For consistency across benchmarks, we fix the power-law parameters to  $\alpha = 0.25$  and  $\beta = 1.75$ , which lie within the range identified as favorable in the grid search. The curves are averaged over five seeds, with shaded regions indicating the standard error.

For the small architecture, Glorot and the baseline perform similarly, while the power-law scheme clearly outperforms both by converging faster and reaching lower final losses. In contrast, for the larger architecture, the differences become much more pronounced. The baseline initialization always plateaus early, struggling to further decrease the loss, whereas Glorot maintains steady descent and power-law achieves significantly lower final losses across all functions.

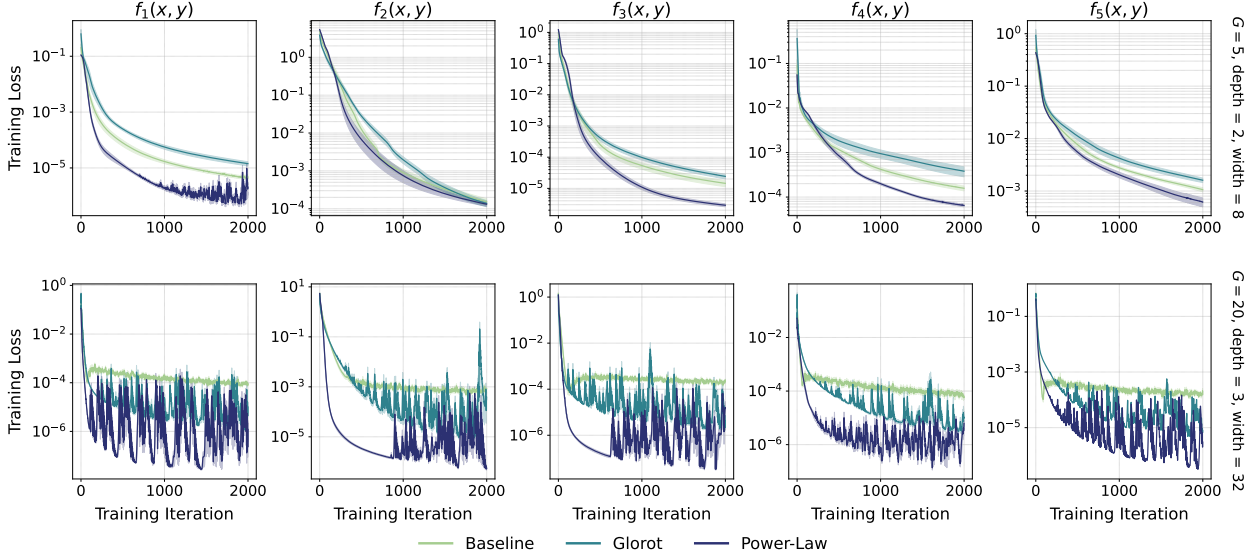


Figure 1: Training loss curves for function fitting benchmarks under baseline, Glorot and power-law initializations. Results are averaged over five seeds, with shaded regions indicating the standard error. Top row: “small” architecture ( $G = 5$ , two hidden layers with 8 neurons each). Bottom row: “large” architecture ( $G = 20$ , three hidden layers with 32 neurons each).

Importantly, the power-law initialization not only reaches the lowest losses but also does so with the steepest initial decrease, indicating faster optimization from the very first iterations. The more pronounced oscillations observed in its curves stem from the fact that the model already reaches very low loss values under a fixed learning rate, leaving no smoothing effect from adaptive adjustments.

We repeat the same analysis for the PDE benchmarks, with results shown in Figure 2. For the smaller architecture, the three initialization schemes perform comparably, though in the Allen–Cahn case the power-law scheme achieves noticeably faster convergence, with lower variance. By contrast, in the larger architecture, the differences are striking: the baseline often stagnates at high loss values, while Glorot initialization provides steady improvement and power-law achieves the lowest overall errors, albeit with oscillations similar to those observed in the function fitting tasks. Overall,

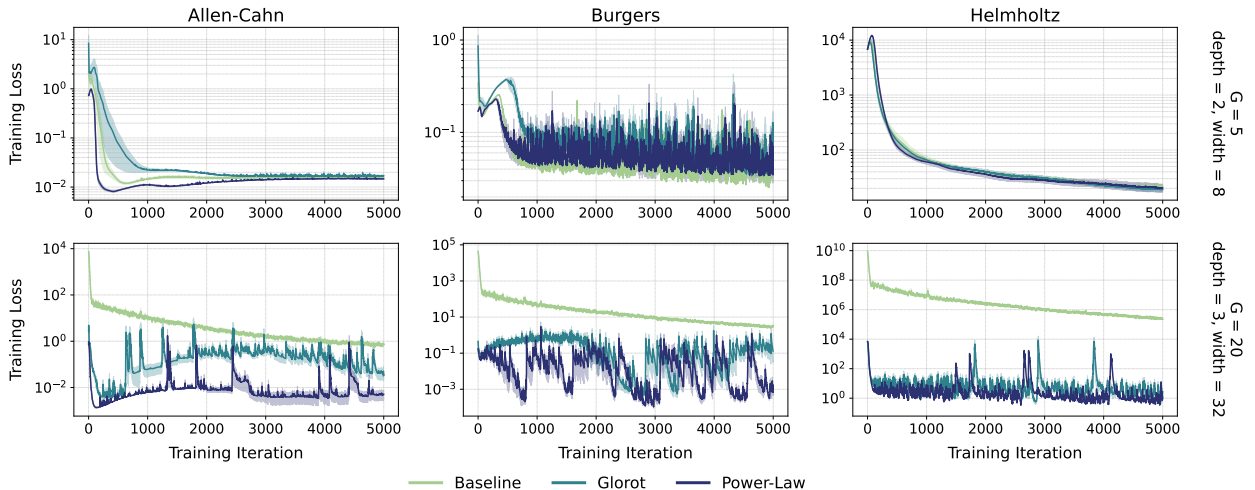


Figure 2: Training loss curves for forward PDE benchmarks under baseline, Glorot, and power-law initializations. Results are averaged over five seeds, with shaded regions indicating the standard error. Top row: “small” architecture ( $G = 5$ , two hidden layers with 8 neurons each). Bottom row: “large” architecture ( $G = 20$ , three hidden layers with 32 neurons each).

the PDE results reinforce the earlier findings, confirming that both Glorot and power-law yield significant gains over the baseline scheme, with the advantage becoming most apparent in parameter-rich models.

To further probe the mechanisms underlying these differences, we complement the loss curve analysis with a study of the NTK dynamics. Since the discrepancies between initialization strategies are most pronounced in larger models, we focus here on the “large” architecture. Figure 3 shows the NTK eigenvalue spectra at initialization, at intermediate training iterations, and at convergence, for function fitting task  $f_3(x, y)$  (results for other targets are consistent and reported in Appendix E.2). The baseline initialization yields a spectrum concentrated at large values that progressively collapses during training, suggesting poor conditioning and limited effective rank. By contrast, both the Glorot- and power-law-based schemes produce spectra that stabilize quickly and remain stable throughout training.

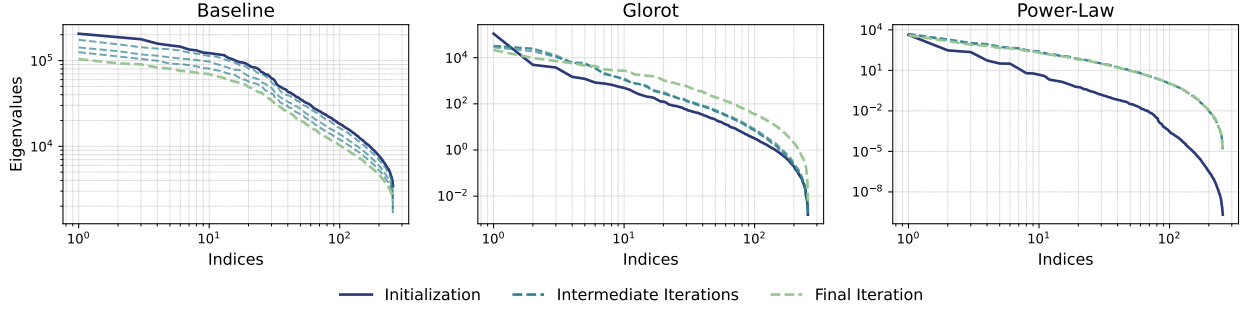


Figure 3: Eigenvalue spectra of the NTK matrix at initialization (solid blue), intermediate iterations (dashed teal), and final iteration (dashed green) for function fitting benchmark  $f_3(x, y)$  under different initialization strategies. Results correspond to the “large” architecture ( $G = 20$ , three hidden layers with 32 neurons each).

We also extend the NTK analysis to PDE benchmarks, focusing on the Allen–Cahn equation as a representative case (results for Burgers and Helmholtz are provided in Appendix E.2). To this end, we adopt the NTK formalism developed for PIML [Wang et al., 2022] and adapt it to account for Residual-Based Attention (RBA) weights [Anagnostopoulos et al., 2024], which are applied in the loss functions studied herein (see Appendix C.2 for details). The resulting kernel is identical to the standard PINN NTK, except that it incorporates the corresponding RBA weights (see Appendix E.1 for the full derivation). Figure 4 shows the NTK eigenvalue spectra separately for the PDE residual term (top row) and the boundary/initial conditions (bottom row).

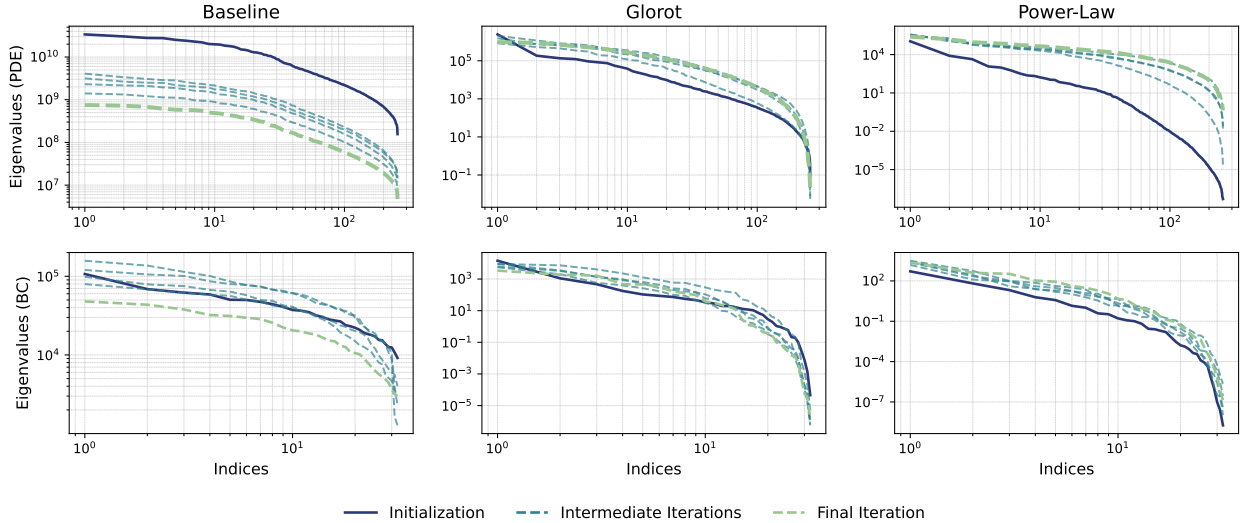


Figure 4: NTK eigenvalue spectra for the Allen–Cahn PDE benchmark under baseline, Glorot, and power-law initializations. Top row: spectra corresponding to the PDE residual term. Bottom row: spectra for the boundary/initial condition terms. Solid lines show the initialization, dashed lines show intermediate iterations, and dotted lines show the final iteration. Results correspond to the “large” architecture ( $G = 20$ , three hidden layers with 32 neurons each).

The PDE residual spectra largely mirror the function fitting case: baseline initialization yields poorly conditioned eigenvalues that collapse over training, while both Glorot and power-law maintain stability. The key difference lies in the boundary/initial condition terms, where Glorot shows some irregularities, though far less severe than the baseline. The power-law scheme stands out as the most consistent, providing stable and well-structured spectra across both PDE residual- and boundary/initial-term components.

### 4.3 Feynman Dataset Benchmarks

As a final benchmark, we turn to a subset of the Feynman dataset, restricted to dimensionless equations. The explicit formulas of the target functions and implementation details are provided in Appendix C.3. We evaluate the baseline, Glorot, and power-law initializations using the same “small” and “large” architectures defined in Section 4.2. Tables 3 and 4 report the results in terms of final training loss and relative  $L^2$  error with respect to the reference solutions, for the small and large settings, respectively.

Table 3: Results on the Feynman benchmark for the “small” architecture ( $G = 5$ , two hidden layers with 8 neurons each). Reported values correspond to median final training loss and relative  $L^2$  error with respect to the reference solution. Best results per equation are shown in bold.

Function	Baseline		Glorot		Power-Law	
	Loss	$L^2$	Loss	$L^2$	Loss	$L^2$
I.6.2	$5.17 \cdot 10^{-3}$	<b><math>4.05 \cdot 10^{-1}</math></b>	$9.86 \cdot 10^{-3}$	$4.22 \cdot 10^{-1}$	<b><math>1.18 \cdot 10^{-3}</math></b>	$4.14 \cdot 10^{-1}$
I.6.2b	$3.58 \cdot 10^{-3}$	<b><math>4.28 \cdot 10^{-1}</math></b>	$8.69 \cdot 10^{-3}$	$5.01 \cdot 10^{-1}$	<b><math>1.97 \cdot 10^{-3}</math></b>	$4.37 \cdot 10^{-1}$
I.12.11	$1.40 \cdot 10^{-5}$	$3.67 \cdot 10^{-3}$	$1.30 \cdot 10^{-5}$	$3.75 \cdot 10^{-3}$	<b><math>1.12 \cdot 10^{-6}</math></b>	<b><math>1.07 \cdot 10^{-3}</math></b>
I.13.12	$2.24 \cdot 10^3$	$1.86 \cdot 10^0$	$3.51 \cdot 10^3$	<b><math>7.65 \cdot 10^{-1}</math></b>	<b><math>1.75 \cdot 10^3</math></b>	$2.36 \cdot 10^0$
I.16.6	$2.62 \cdot 10^{-4}$	$3.55 \cdot 10^{-2}$	$2.94 \cdot 10^{-4}$	$3.63 \cdot 10^{-2}$	<b><math>1.19 \cdot 10^{-4}</math></b>	<b><math>2.92 \cdot 10^{-2}</math></b>
I.18.4	$1.39 \cdot 10^3$	<b><math>1.00 \cdot 10^0</math></b>	$2.31 \cdot 10^3$	<b><math>1.00 \cdot 10^0</math></b>	<b><math>1.04 \cdot 10^3</math></b>	<b><math>1.00 \cdot 10^0</math></b>
I.26.2	$5.00 \cdot 10^{-6}$	$7.21 \cdot 10^{-3}$	$1.40 \cdot 10^{-5}$	$1.19 \cdot 10^{-2}$	<b><math>9.99 \cdot 10^{-7}</math></b>	<b><math>3.13 \cdot 10^{-3}</math></b>
I.27.6	<b><math>1.87 \cdot 10^{-3}</math></b>	<b><math>1.00 \cdot 10^0</math></b>	$1.24 \cdot 10^{-1}$	<b><math>1.00 \cdot 10^0</math></b>	$1.77 \cdot 10^{-1}$	<b><math>1.00 \cdot 10^0</math></b>
I.29.16	$1.05 \cdot 10^{-4}$	$1.14 \cdot 10^{-2}$	$1.22 \cdot 10^{-4}$	$1.24 \cdot 10^{-2}$	<b><math>3.14 \cdot 10^{-5}</math></b>	<b><math>6.83 \cdot 10^{-3}</math></b>
I.30.3	$4.00 \cdot 10^{-6}$	$4.62 \cdot 10^{-3}$	$9.00 \cdot 10^{-6}$	$6.84 \cdot 10^{-3}$	<b><math>4.88 \cdot 10^{-7}</math></b>	<b><math>1.73 \cdot 10^{-3}</math></b>
I.40.1	$1.30 \cdot 10^{-5}$	$4.76 \cdot 10^{-3}$	$3.90 \cdot 10^{-5}$	$8.11 \cdot 10^{-3}$	<b><math>1.74 \cdot 10^{-6}</math></b>	<b><math>1.81 \cdot 10^{-3}</math></b>
I.50.26	$1.40 \cdot 10^{-5}$	$4.07 \cdot 10^{-3}$	$1.00 \cdot 10^{-5}$	$3.47 \cdot 10^{-3}$	<b><math>1.17 \cdot 10^{-6}</math></b>	<b><math>1.20 \cdot 10^{-3}</math></b>
II.2.42	$1.52 \cdot 10^{-4}$	$4.46 \cdot 10^{-3}$	$2.50 \cdot 10^{-5}$	$7.74 \cdot 10^{-3}$	<b><math>8.49 \cdot 10^{-7}</math></b>	<b><math>1.44 \cdot 10^{-3}</math></b>
II.6.15a	$6.00 \cdot 10^{-6}$	$7.35 \cdot 10^{-2}$	$1.80 \cdot 10^{-5}$	$1.16 \cdot 10^{-1}$	<b><math>4.97 \cdot 10^{-7}</math></b>	<b><math>1.89 \cdot 10^{-2}</math></b>
II.11.7	$2.70 \cdot 10^{-5}$	$1.03 \cdot 10^{-2}$	$6.10 \cdot 10^{-5}$	$1.44 \cdot 10^{-2}$	<b><math>3.58 \cdot 10^{-6}</math></b>	<b><math>4.08 \cdot 10^{-3}</math></b>
II.11.27	$4.00 \cdot 10^{-6}$	$6.20 \cdot 10^{-3}$	$1.50 \cdot 10^{-5}$	$1.21 \cdot 10^{-2}$	<b><math>7.17 \cdot 10^{-7}</math></b>	<b><math>2.72 \cdot 10^{-3}</math></b>
II.35.18	$3.00 \cdot 10^{-6}$	$7.61 \cdot 10^{-3}$	$1.10 \cdot 10^{-5}$	$1.38 \cdot 10^{-2}$	<b><math>1.84 \cdot 10^{-7}</math></b>	<b><math>1.48 \cdot 10^{-3}</math></b>
II.36.38	$3.50 \cdot 10^{-5}$	$1.17 \cdot 10^{-2}$	$6.50 \cdot 10^{-5}$	$1.57 \cdot 10^{-2}$	<b><math>2.71 \cdot 10^{-6}</math></b>	<b><math>3.43 \cdot 10^{-3}</math></b>
III.10.19	$1.40 \cdot 10^{-5}$	$3.14 \cdot 10^{-3}$	$1.50 \cdot 10^{-5}$	$2.90 \cdot 10^{-3}$	<b><math>8.26 \cdot 10^{-6}</math></b>	<b><math>2.24 \cdot 10^{-3}</math></b>
III.17.37	$2.60 \cdot 10^{-5}$	$1.05 \cdot 10^{-2}$	$5.30 \cdot 10^{-5}$	$1.41 \cdot 10^{-2}$	<b><math>4.35 \cdot 10^{-6}</math></b>	<b><math>4.37 \cdot 10^{-3}</math></b>

The results confirm the same overall trends observed in the earlier benchmarks. In both settings, power-law initialization achieves the best performance on the majority of equations, often by large margins in terms of both final training loss and relative  $L^2$  error. Glorot initialization also provides substantial improvements over the baseline, particularly in the large architecture, where it consistently narrows the gap to power-law. A comparison between Tables 3 and 4 further highlights the role of initialization: with Glorot and power-law, the richer architecture is able to drive the loss down by several orders of magnitude and simultaneously reduce the  $L^2$  error, whereas under the baseline initialization, performance often degrades when moving from the small to the large setting.

## 5 Conclusion

In this work, we proposed and systematically evaluated new initialization strategies for spline-based KANs. Specifically, we introduced two theory-driven schemes inspired by LeCun and Glorot, including a variant with batch-normalized basis functions, as well as an empirical family of power-law initializations with tunable exponents. Through large-scale grid searches, training dynamics analysis, and evaluations on both PDE and function fitting benchmarks, we showed that initialization plays a crucial role in KAN performance. Our results demonstrate that while LeCun-inspired schemes

Table 4: Results on the Feynman benchmark for the “large” architecture ( $G = 20$ , three hidden layers with 32 neurons each). Reported values correspond to median final training loss and relative  $L^2$  error with respect to the reference solution. Best results per equation are shown in bold.

Function	Baseline		Glorot		Power-Law	
	Loss	$L^2$	Loss	$L^2$	Loss	$L^2$
I.6.2	$1.09 \cdot 10^{-3}$	$1.51 \cdot 10^0$	$4.80 \cdot 10^{-5}$	$4.19 \cdot 10^{-1}$	<b><math>5.20 \cdot 10^{-6}</math></b>	<b><math>3.85 \cdot 10^{-1}</math></b>
I.6.2b	$1.36 \cdot 10^{-3}$	$1.64 \cdot 10^0$	$7.60 \cdot 10^{-5}$	$5.80 \cdot 10^{-1}$	<b><math>2.18 \cdot 10^{-6}</math></b>	<b><math>4.59 \cdot 10^{-1}</math></b>
I.12.11	$1.64 \cdot 10^{-4}$	$3.77 \cdot 10^{-1}$	$3.00 \cdot 10^{-6}$	$1.47 \cdot 10^{-3}$	<b><math>2.16 \cdot 10^{-8}</math></b>	<b><math>1.66 \cdot 10^{-4}</math></b>
I.13.12	$2.70 \cdot 10^3$	$3.08 \cdot 10^0$	$2.81 \cdot 10^3$	<b><math>1.11 \cdot 10^0</math></b>	<b><math>2.53 \cdot 10^{-1}</math></b>	$5.49 \cdot 10^0$
I.16.6	$1.63 \cdot 10^{-4}$	$6.31 \cdot 10^{-1}$	$6.00 \cdot 10^{-6}$	$1.63 \cdot 10^{-2}$	<b><math>1.09 \cdot 10^{-6}</math></b>	<b><math>1.48 \cdot 10^{-2}</math></b>
I.18.4	$2.67 \cdot 10^2$	<b><math>1.00 \cdot 10^0</math></b>	$1.53 \cdot 10^3$	<b><math>1.00 \cdot 10^0</math></b>	<b><math>4.15 \cdot 10^{-2}</math></b>	<b><math>1.00 \cdot 10^0</math></b>
I.26.2	$1.01 \cdot 10^{-4}$	$1.10 \cdot 10^0$	$7.00 \cdot 10^{-6}$	$8.98 \cdot 10^{-3}$	<b><math>1.72 \cdot 10^{-7}</math></b>	<b><math>1.25 \cdot 10^{-3}</math></b>
I.27.6	$3.33 \cdot 10^{-3}$	<b><math>1.00 \cdot 10^0</math></b>	$1.85 \cdot 10^{-4}$	<b><math>1.00 \cdot 10^0</math></b>	<b><math>8.93 \cdot 10^{-5}</math></b>	<b><math>1.00 \cdot 10^0</math></b>
I.29.16	$2.01 \cdot 10^{-4}$	$4.45 \cdot 10^{-1}$	$1.20 \cdot 10^{-5}$	$6.28 \cdot 10^{-3}$	<b><math>2.06 \cdot 10^{-7}</math></b>	<b><math>2.57 \cdot 10^{-3}</math></b>
I.30.3	$1.18 \cdot 10^{-4}$	$7.72 \cdot 10^{-1}$	$1.00 \cdot 10^{-6}$	$2.92 \cdot 10^{-3}$	<b><math>2.17 \cdot 10^{-8}</math></b>	<b><math>4.17 \cdot 10^{-4}</math></b>
I.40.1	$2.26 \cdot 10^{-4}$	$6.70 \cdot 10^{-1}$	$5.00 \cdot 10^{-6}$	$3.39 \cdot 10^{-3}$	<b><math>1.41 \cdot 10^{-7}</math></b>	<b><math>6.17 \cdot 10^{-4}</math></b>
I.50.26	$2.03 \cdot 10^{-4}$	$4.38 \cdot 10^{-1}$	$2.00 \cdot 10^{-6}$	$1.50 \cdot 10^{-3}$	<b><math>3.70 \cdot 10^{-8}</math></b>	<b><math>2.25 \cdot 10^{-4}</math></b>
II.2.42	$1.52 \cdot 10^{-4}$	$6.86 \cdot 10^{-1}$	$4.00 \cdot 10^{-6}$	$2.62 \cdot 10^{-3}$	<b><math>8.54 \cdot 10^{-8}</math></b>	<b><math>4.98 \cdot 10^{-4}</math></b>
II.6.15a	$6.60 \cdot 10^{-5}$	$7.60 \cdot 10^0$	$2.00 \cdot 10^{-6}$	$5.47 \cdot 10^{-2}$	<b><math>8.13 \cdot 10^{-9}</math></b>	<b><math>4.40 \cdot 10^{-3}</math></b>
II.11.7	$1.75 \cdot 10^{-4}$	$9.78 \cdot 10^{-1}$	$1.10 \cdot 10^{-5}$	$1.01 \cdot 10^{-2}$	<b><math>1.80 \cdot 10^{-7}</math></b>	<b><math>3.00 \cdot 10^{-3}</math></b>
II.11.27	$8.80 \cdot 10^{-5}$	$1.04 \cdot 10^0$	$1.00 \cdot 10^{-6}$	$3.76 \cdot 10^{-3}$	<b><math>1.54 \cdot 10^{-7}</math></b>	<b><math>1.95 \cdot 10^{-3}</math></b>
II.35.18	$7.40 \cdot 10^{-5}$	$1.19 \cdot 10^0$	$6.00 \cdot 10^{-6}$	$1.18 \cdot 10^{-2}$	<b><math>2.95 \cdot 10^{-8}</math></b>	<b><math>7.77 \cdot 10^{-4}</math></b>
II.36.38	$1.93 \cdot 10^{-4}$	$9.48 \cdot 10^{-1}$	$8.00 \cdot 10^{-6}$	$1.11 \cdot 10^{-2}$	<b><math>3.05 \cdot 10^{-7}</math></b>	<b><math>4.92 \cdot 10^{-3}</math></b>
III.10.19	$1.81 \cdot 10^{-4}$	$2.74 \cdot 10^{-1}$	$1.00 \cdot 10^{-6}$	$9.89 \cdot 10^{-4}$	<b><math>9.87 \cdot 10^{-9}</math></b>	<b><math>8.70 \cdot 10^{-5}</math></b>
III.17.37	$1.45 \cdot 10^{-4}$	$9.10 \cdot 10^{-1}$	$4.90 \cdot 10^{-5}$	$1.31 \cdot 10^{-2}$	<b><math>6.45 \cdot 10^{-6}</math></b>	<b><math>5.14 \cdot 10^{-3}</math></b>

offer limited benefits, Glorot-inspired initialization emerges as a strong candidate for parameter-rich architectures, and the empirical power-law family provides the most robust improvements overall, achieving faster convergence and lower errors across benchmarks. These findings highlight initialization as a key component of training KANs and identify effective practical strategies for the process.

## 5.1 Limitations and Future Work

While our study establishes the importance of initialization in spline-based KANs, it also comes with limitations. Our power-law scheme, although empirically effective, currently lacks a rigorous theoretical foundation, and understanding why specific exponent ranges perform well remains an open question. Moreover, although we considered both supervised function fitting and physics-informed PDE benchmarks, further exploration in other domains such as reinforcement learning or generative modeling could provide additional insights. Addressing these limitations offers natural directions for future work, including deriving principled theory for power-law initialization, investigating transferability across KAN variants (e.g., Chebyshev-based or residual-free forms), and exploring initialization strategies in conjunction with adaptive optimization techniques.

## Reproducibility Statement

The full code (including selected seeds for each experiment) and the processed data from the grid-search experiments are publicly available at [https://github.com/srigas/KAN\\_Initialization\\_Schemes](https://github.com/srigas/KAN_Initialization_Schemes).

---

## References

- Ziming Liu, Yixuan Wang, Sachin Vaidya, Fabian Ruehle, James Halverson, Marin Soljacic, Thomas Y. Hou, and Max Tegmark. KAN: Kolmogorov–Arnold networks. In *The Thirteenth International Conference on Learning Representations*, 2025. URL <https://openreview.net/forum?id=0zo7qJ5vZi>.
- A. K. Kolmogorov. On the representation of continuous functions of several variables by superposition of continuous functions of one variable and addition. *Doklady Akademii Nauk SSSR*, 114:369–373, 1957.
- Runpeng Yu, Weihao Yu, and Xinchao Wang. KAN or MLP: A fairer comparison, 2024. URL <https://arxiv.org/abs/2407.16674>.
- Eleonora Poeta, Flavio Giobergia, Eliana Pastor, Tania Cerquitelli, and Elena Baralis. A benchmarking study of Kolmogorov–Arnold networks on tabular data. In *2024 IEEE 18th International Conference on Application of Information and Communication Technologies (AICT)*, pages 1–6, 2024. doi:10.1109/AICT61888.2024.10740444.
- Ziming Liu, Pingchuan Ma, Yixuan Wang, Wojciech Matusik, and Max Tegmark. Kan 2.0: Kolmogorov–Arnold networks meet science, 2024. URL <https://arxiv.org/abs/2408.10205>.
- Khemraj Shukla, Juan Diego Toscano, Zhicheng Wang, Zongren Zou, and George Em Karniadakis. A comprehensive and FAIR comparison between MLP and KAN representations for differential equations and operator networks. *Comput. Methods Appl. Mech. Eng.*, 431:117290, 2024. doi:<https://doi.org/10.1016/j.cma.2024.117290>. URL <https://www.sciencedirect.com/science/article/pii/S0045782524005462>.
- Spyros Rigas, Michalis Papachristou, Theofilos Papadopoulos, Fotios Anagnostopoulos, and Georgios Alexandridis. Adaptive training of grid-dependent physics-informed Kolmogorov–Arnold networks. *IEEE Access*, 12:176982–176998, 2024. doi:10.1109/ACCESS.2024.3504962.
- Yizheng Wang, Jia Sun, Jinshuai Bai, Cosmin Anitescu, Mohammad Sadegh Eshaghi, Xiaoying Zhuang, Timon Rabczuk, and Yinghua Liu. Kolmogorov–Arnold-informed neural network: A physics-informed deep learning framework for solving forward and inverse problems based on Kolmogorov–Arnold networks. *Comput. Methods Appl. Mech. Eng.*, 433:117518, 2025a. doi:<https://doi.org/10.1016/j.cma.2024.117518>. URL <https://www.sciencedirect.com/science/article/pii/S0045782524007722>.
- Diab W. Abueidda, Panos Pantidis, and Mostafa E. Mobasher. DeepOKAN: Deep operator network based on Kolmogorov Arnold networks for mechanics problems. *Comput. Methods Appl. Mech. Eng.*, 436:117699, 2025. doi:<https://doi.org/10.1016/j.cma.2024.117699>. URL <https://www.sciencedirect.com/science/article/pii/S0045782524009538>.
- Amanda A. Howard, Bruno Jacob, Sarah H. Murphy, Alexander Heinlein, and Panos Stinis. Finite basis Kolmogorov–Arnold networks: domain decomposition for data-driven and physics-informed problems, 2024. URL <https://arxiv.org/abs/2406.19662>.
- Aakash Kundu, Aritra Sarkar, and Abhishek Sadhu. KANQAS: Kolmogorov–Arnold network for quantum architecture search. *EPJ Quantum Technol.*, 11:76, 2024. doi:<https://doi.org/10.1140/epjqt/s40507-024-00289-z>.
- Ali Kashefi. Kolmogorov–Arnold PointNet: Deep learning for prediction of fluid fields on irregular geometries. *Comput. Methods Appl. Mech. Eng.*, 439:117888, 2025. doi:<https://doi.org/10.1016/j.cma.2025.117888>. URL <https://www.sciencedirect.com/science/article/pii/S0045782525001604>.
- Xianyang Zhang and Huijuan Zhou. Generalization bounds and model complexity for Kolmogorov–Arnold networks. In *The Thirteenth International Conference on Learning Representations*, 2025. URL <https://openreview.net/forum?id=q5zMyAUhGx>.
- Tal Alter, Raz Lapid, and Moshe Sipper. On the robustness of Kolmogorov–Arnold networks: An adversarial perspective. *Transactions on Machine Learning Research*, 2025. URL <https://openreview.net/forum?id=uafxqhImPM>.
- Yixuan Wang, Jonathan W. Siegel, Ziming Liu, and Thomas Y. Hou. On the expressiveness and spectral bias of KANs. In *The Thirteenth International Conference on Learning Representations*, 2025b. URL <https://openreview.net/forum?id=ydlDRUuGm9>.
- Spyros Rigas, Michalis Papachristou, Fotios Anagnostopoulos, and Georgios Alexandridis. Towards deep physics-informed Kolmogorov–Arnold networks. Under review, 2025.
- Dmytro Mishkin and Jiri Matas. All you need is a good init. In *4th International Conference on Learning Representations, ICLR 2016*, 2016. URL <https://arxiv.org/abs/1511.06422>.
- Maciej Skorski, Alessandro Temperoni, and Martin Theobald. Revisiting weight initialization of deep neural networks. In *Proceedings of The 13th Asian Conference on Machine Learning*, volume 157, pages 1192–1207, 2021. URL <https://proceedings.mlr.press/v157/skorski21a.html>.

- 
- Xavier Glorot and Yoshua Bengio. Understanding the difficulty of training deep feedforward neural networks. In *Proceedings of the Thirteenth International Conference on Artificial Intelligence and Statistics*, volume 9, pages 249–256, 2010. URL <https://proceedings.mlr.press/v9/glorot10a.html>.
- Xiao Shi Huang, Felipe Perez, Jimmy Ba, and Maksims Volkovs. Improving transformer optimization through better initialization. In *Proceedings of the 37th International Conference on Machine Learning*, volume 119, pages 4475–4483, 2020. URL <https://proceedings.mlr.press/v119/huang20f.html>.
- Kaiming He, Xiangyu Zhang, Shaoqing Ren, and Jian Sun. Delving deep into rectifiers: Surpassing human-level performance on ImageNet classification. In *2015 IEEE International Conference on Computer Vision (ICCV)*, pages 1026–1034, 2015. doi:10.1109/ICCV.2015.123.
- Yann LeCun, Leon Bottou, Genevieve B. Orr, and Klaus-Robert Müller. Efficient backprop. In Genevieve B. Orr and Klaus-Robert Müller, editors, *Neural Networks: Tricks of the Trade*, pages 9–50. Springer, 1998. ISBN 978-3-540-49430-0. doi:10.1007/3-540-49430-8\_2.
- Sergey Ioffe and Christian Szegedy. Batch normalization: accelerating deep network training by reducing internal covariate shift. In *Proceedings of the 32nd International Conference on International Conference on Machine Learning - Volume 37*, page 448–456, 2015.
- Arthur Jacot, Franck Gabriel, and Clement Hongler. Neural Tangent Kernel: Convergence and generalization in neural networks. In *Advances in Neural Information Processing Systems*, volume 31, 2018. URL [https://proceedings.neurips.cc/paper\\_files/paper/2018/file/5a4be1fa34e62bb8a6ec6b91d2462f5a-Paper.pdf](https://proceedings.neurips.cc/paper_files/paper/2018/file/5a4be1fa34e62bb8a6ec6b91d2462f5a-Paper.pdf).
- Sifan Wang, Xinling Yu, and Paris Perdikaris. When and why pinns fail to train: A neural tangent kernel perspective. *Journal of Computational Physics*, 449:110768, 2022. doi:10.1016/j.jcp.2021.110768.
- Silviu-Marian Udrescu and Max Tegmark. AI Feynman: A physics-inspired method for symbolic regression. *Science Advances*, 6(16):eaay2631, 2020. doi:10.1126/sciadv.aay2631.
- Leonardo Ferreira Guilhoto and Paris Perdikaris. Deep learning alternatives of the Kolmogorov superposition theorem. In *The Thirteenth International Conference on Learning Representations*, 2025. URL <https://openreview.net/forum?id=SyVPiehSbg>.
- M. Raissi, P. Perdikaris, and G.E. Karniadakis. Physics-informed neural networks: A deep learning framework for solving forward and inverse problems involving nonlinear partial differential equations. *J. Comput. Phys.*, 378:686–707, 2019. doi:<https://doi.org/10.1016/j.jcp.2018.10.045>. URL <https://www.sciencedirect.com/science/article/pii/S0021999118307125>.
- James Bradbury, Roy Frostig, Peter Hawkins, Matthew James Johnson, Chris Leary, Dougal Maclaurin, George Necula, Adam Paszke, Jake VanderPlas, Skye Wanderman-Milne, and Qiao Zhang. JAX: composable transformations of Python+NumPy programs, 2018. URL <http://github.com/jax-ml/jax>.
- Spyros Rigas and Michalis Papachristou. jaxKAN: A unified JAX framework for Kolmogorov–Arnold networks. *Journal of Open Source Software*, 10(108):7830, 2025. doi:10.21105/joss.07830. URL <https://doi.org/10.21105/joss.07830>.
- Sifan Wang, Bowen Li, Yuhang Chen, and Paris Perdikaris. Piratenets: Physics-informed deep learning with residual adaptive networks. *Journal of Machine Learning Research*, 25(402):1–51, 2024.
- Sokratis J. Anagnostopoulos, Juan Diego Toscano, Nikolaos Stergiopoulos, and George Em Karniadakis. Residual-based attention in physics-informed neural networks. *Computer Methods in Applied Mechanics and Engineering*, 421:116805, 2024. doi:10.1016/j.cma.2024.116805.

---

## A Derivation of LeCun-inspired Initialization Scheme

In this appendix, we provide a derivation of Eqs. (2) from the main text. Assuming statistical independence between each term in the outer sum of Eq. (1) and requiring the output variance to match the input variance, one finds

$$\text{Var}(x_i) = n_{\text{in}} \text{Var} \left[ r_{ji} R(x_i) + c_{ji} \sum_{m=1}^{G+k} b_{jim} B_m(x_i) \right], \quad (8)$$

where the right-hand side contains the variance of a sum of  $G + k + 1$  terms: one residual term and  $G + k$  spline basis terms. We adopt a simplifying assumption that the total variance is approximately equipartitioned across all components,<sup>4</sup> allowing us to bypass pairwise covariance terms. This leads to the following expressions for the residual and spline basis terms, respectively:

$$\frac{\text{Var}(x_i)}{G + k + 1} = n_{\text{in}} \text{Var}[r_{ji} R(x_i)], \quad \frac{\text{Var}(x_i)}{G + k + 1} = n_{\text{in}} \text{Var}[b_{jim} B_m(x_i)]. \quad (9)$$

Since the trainable weights  $r_{ji}$  are independent of the residual function  $R(x_i)$ , the variance of their product becomes

$$\begin{aligned} \text{Var}[r_{ji} R(x_i)] &= \underbrace{\mathbb{E}^2(r_{ji})}_{=0} \text{Var}[R(x_i)] + \mathbb{E}^2[R(x_i)] \text{Var}(r_{ji}) + \text{Var}(r_{ji}) \text{Var}[R(x_i)] \\ &= \text{Var}(r_{ji}) \{\text{Var}[R(x_i)] + \mathbb{E}^2[R(x_i)]\} = \sigma_r^2 \mathbb{E}[R^2(x_i)] \end{aligned} \quad (10)$$

and, in a completely analogous manner, we find

$$\text{Var}[b_{jim} B_m(x_i)] = \sigma_b^2 \mathbb{E}[B_m^2(x_i)]. \quad (11)$$

Substitution of the expressions of Eqs. (10), (11) into Eqs. (9) yields Eq. (2) from Section 3.1.

---

<sup>4</sup>This assumption does not necessarily hold in general. For example, one could consider a 50%–50% split between the residual and basis function terms. We experimented with this alternative and found that it yielded poorer results compared to the variance partitioning that leads to Eqs. (2).

## B Derivation of Glorot-inspired Initialization Scheme

In this appendix, we derive Eqs. (5) from the main text. Unlike the LeCun-inspired scheme, which focuses solely on variance preservation in the forward pass, the Glorot principle [Glorot and Bengio, 2010] requires that the variance of both activations and backpropagated gradients remain constant across layers. For analytical tractability, and following the standard assumption in this setting, we further approximate these constant values by unity,

$$\text{Var}(x_i) = \text{Var}(y_i) \approx 1, \quad \text{Var}(\delta x_i) = \text{Var}(\delta y_i) \approx 1, \quad (12)$$

where  $\delta x_i = \partial \mathcal{L} / \partial x_i$  and  $\delta y_j = \partial \mathcal{L} / \partial y_j$ , with  $\mathcal{L}$  denoting the loss function. This approximation is consistent with the common assumption of i.i.d. inputs with zero mean and unit variance. In practice, when this assumption does not hold, an additional gain factor can be introduced to rescale the initialization, as is standard in frameworks such as PyTorch.

Using the result from Appendix A together with the first condition of Eq. (12), the constraints for variance preservation in the forward pass can be written as

$$1 = (G + k + 1) n_{\text{in}} \sigma_r^2 \mu_R^{(0)}, \quad 1 = (G + k + 1) n_{\text{in}} \sigma_b^2 \mu_B^{(0)}, \quad (13)$$

where  $\mu_R^{(0)} = \mathbb{E}[R(x_i)^2]$  and  $\mu_B^{(0)} = \mathbb{E}[B_m(x_i)^2]$  as defined in Eq. (3).

For the backward pass, differentiating Eq. (1) with respect to  $x_i$  gives

$$\frac{\partial y_j}{\partial x_i} = r_{ji} R'(x_i) + c_{ji} \sum_{m=1}^{G+k} b_{jim} B'_m(x_i), \quad (14)$$

Setting  $c_{ji} = 1$ , the chain rule yields

$$\delta x_i = \sum_{j=1}^{n_{\text{out}}} \frac{\partial y_j}{\partial x_i} \delta y_j = \underbrace{\sum_{j=1}^{n_{\text{out}}} r_{ji} R'(x_i) \delta y_j}_{\text{residual contribution}} + \underbrace{\sum_{m=1}^{G+k} \sum_{j=1}^{n_{\text{out}}} b_{jim} B'_m(x_i) \delta y_j}_{m\text{-th spline contribution}}, \quad (15)$$

and applying the second condition of Eq. (12) gives

$$1 = n_{\text{out}} \text{Var} \left[ r_{ji} R'(x_i) + \sum_{m=1}^{G+k} b_{jim} B'_m(x_i) \right], \quad (16)$$

where we have adopted the standard Glorot assumptions: the  $\delta y_j$  are zero-mean, mutually independent, and independent of weights and inputs. At this point we may again equipartition the total variance across the  $(G+k+1)$  components (one residual term and  $G+k$  spline terms), exactly mirroring the forward-pass treatment. This leads to

$$1 = (G + k + 1) n_{\text{out}} \text{Var}[r_{ji} R'(x_i)], \quad 1 = (G + k + 1) n_{\text{out}} \text{Var}[b_{jim} B'_m(x_i)], \quad (17)$$

and, following the same arguments as in Appendix A, we find

$$1 = (G + k + 1) n_{\text{out}} \sigma_r^2 \mu_R^{(1)}, \quad 1 = (G + k + 1) n_{\text{out}} \sigma_b^2 \mu_B^{(1)}, \quad (18)$$

where  $\mu_R^{(1)} = \mathbb{E}[R'(x_i)^2]$  and  $\mu_B^{(1)} = \mathbb{E}[B'_m(x_i)^2]$  as defined in Eq. (6).

---

Equations (13) and (17) are the forward- and backward-pass constraints, respectively. Balancing them in the Glorot manner (i.e., by harmonic averaging) yields the standard deviations in Eq. (5) of the main text. As a sanity check, consider an MLP: the residual term is absent, and the linear layer followed by a nonlinearity can be viewed as a single basis function. For the common hyperbolic tangent activation,  $\mu_B^{(0)} \approx \mu_B^{(1)} \approx 1$  [Glorot and Bengio, 2010], so our scheme reduces to

$$\sigma_b = \sqrt{\underbrace{\frac{1}{G+k+1}}_{=1} \cdot \underbrace{\frac{2}{n_{\text{in}} \underbrace{\mu_B^{(0)}}_{\approx 1} + n_{\text{out}} \underbrace{\mu_B^{(1)}}_{\approx 1}}} = \sqrt{\frac{2}{n_{\text{in}} + n_{\text{out}}}}, \quad (19)$$

which recovers the classical Glorot initialization.

## C Implementation Details

This appendix provides the full specifications of the benchmarks used in our experiments, including the functional forms of the target problems, training setups, and data generation procedures. We separate the discussion into three parts: function fitting, forward PDE problems and the Feynman dataset.

### C.1 Function Fitting

For the function fitting experiments of Section 4.1 and Section 4.2, we study five two-dimensional functions ranging from simple expressions to more complex, nonlinear, or piecewise-defined forms. Specifically, we consider the following functions in the  $[-1, 1] \times [-1, 1]$  domain:

- $f_1(x, y) = xy$
- $f_2(x, y) = \exp(\sin(\pi x) + y^2)$
- $f_3(x, y) = I_1(x) + \exp[\exp(-|y|)I_1(y)] + \sin(xy)$
- $f_4(x, y) = S[f_3(x, y) + \text{erf}^{-1}(y)] \times C[f_3(x, y) + \text{erf}^{-1}(y)]$
- $f_5(x, y) = y \cdot \text{sgn}(0.5 - x) + \text{erf}(x) \cdot \min\left(xy, \frac{1}{xy}\right)$

where  $I_1(x)$  is the modified Bessel function of first order,  $\text{sgn}(x)$  is the sign function,  $\text{erf}(x)$  is the error function and  $S(x), C(x)$  are the Fresnel integral functions defined as

$$S(x) = \int_0^x \sin\left(\frac{\pi t^2}{2}\right) dt, \quad C(x) = \int_0^x \cos\left(\frac{\pi t^2}{2}\right) dt. \quad (20)$$

The reference surfaces for these functions are shown in Figure 5.

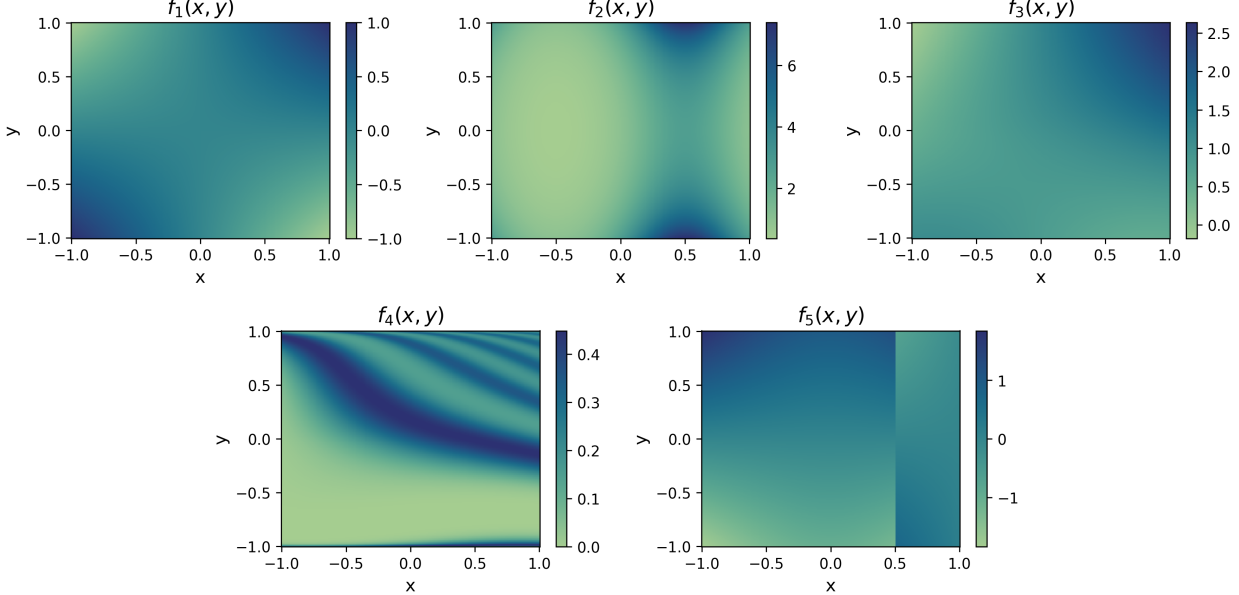


Figure 5: Reference surfaces for the five two-dimensional target functions  $f_1$  through  $f_5$  used in the function fitting experiments.

The KAN models used to fit these functions utilize spline basis functions of order  $k = 3$ , defined over an augmented, uniform grid within the  $[-1, 1]$  domain [Liu et al., 2025]. Training is performed using the Adam optimizer with a fixed learning rate of  $10^{-3}$ , with the objective of minimizing the mean squared error between the predicted and reference function values. For each target function  $f_i(x, y)$ , with  $i = 1, \dots, 5$ , we generate 4,000 random input samples

uniformly distributed over the domain  $[-1, 1] \times [-1, 1]$ , and calculate the corresponding outputs to serve as ground truth during training. To compute the relative  $L^2$  error between the model predictions and reference solutions, we evaluate all trained models on a uniform  $200 \times 200$  grid covering the same domain.

## C.2 Forward PDE Problems

In addition to function fitting, we consider three representative forward PDEs commonly used as PIML benchmarks. For each case, we specify the governing equation, domain and boundary/initial conditions.

**Allen–Cahn equation.** We solve the Allen–Cahn equation on  $(t, x) \in [0, 1] \times [-1, 1]$ :

$$u_t(t, x) - D u_{xx}(t, x) - c(u(t, x) - u(t, x)^3) = 0, \quad (21)$$

with diffusion coefficient  $D = 10^{-4}$  and reaction strength  $c = 5$ . The initial and boundary conditions are

$$u(0, x) = x^2 \cos(\pi x), \quad x \in [-1, 1], \quad (22)$$

$$u(t, -1) = u(t, 1) = -1, \quad t \in [0, 1]. \quad (23)$$

Since the Allen–Cahn equation has no analytic closed-form solution, we use the reference solution used in Wang et al. [2024], which is depicted in the left plot of Fig. 6.

**Burgers' equation.** We solve the viscous Burgers' equation on  $(t, x) \in [0, 1] \times [-1, 1]$ :

$$u_t(t, x) + u(t, x) u_x(t, x) - \nu u_{xx}(t, x) = 0, \quad (24)$$

for  $\nu = 0.01/\pi$ , with initial and boundary conditions

$$u(0, x) = -\sin(\pi x), \quad x \in [-1, 1], \quad (25)$$

$$u(t, -1) = u(t, 1) = 0, \quad t \in [0, 1]. \quad (26)$$

Similar to the Allen–Cahn equation, Burger's equation has no analytic closed-form solution, therefore we use the reference solution used in Wang et al. [2024], which is depicted in the middle plot of Fig. 6.

**Helmholtz equation.** We solve a two-dimensional Helmholtz problem on  $(x, y) \in [-1, 1]^2$  with unit wavenumber and a separable sinusoidal source:

$$u_{xx}(x, y) + u_{yy}(x, y) + u(x, y) = f(x, y), \quad (27)$$

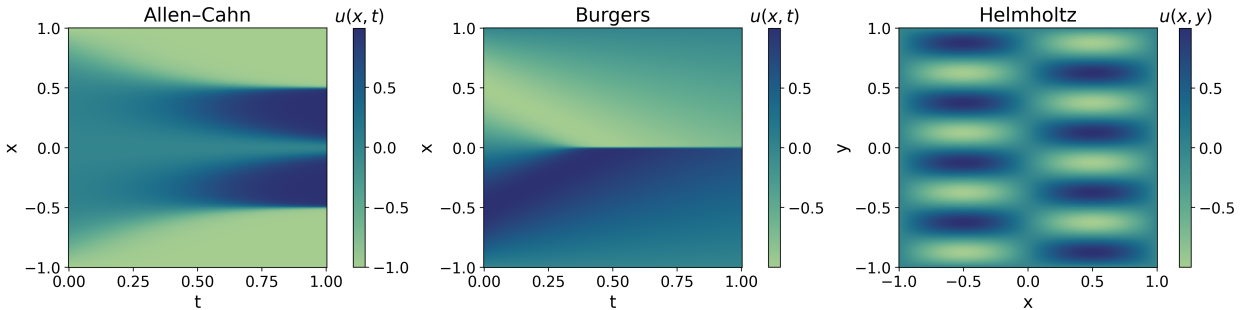


Figure 6: Reference solutions for the three PDE problems considered.

where

$$f(x, y) = (1 - \pi^2(a_1^2 + a_2^2)) \sin(\pi a_1 x) \sin(\pi a_2 y), \quad (28)$$

and  $a_1 = 1$  and  $a_2 = 4$ . We consider homogeneous Dirichlet boundary conditions:

$$u(x, y) = 0 \quad \text{for } (x, y) \in \partial([-1, 1]^2). \quad (29)$$

The analytic solution to this PDE problem is

$$u_{\text{ref}}(x, y) = \sin(\pi x) \sin(4\pi y), \quad (30)$$

and is depicted in the right plot of Fig. 6 for  $x, y$  sampled on a uniform  $512 \times 512$  grid.

The PDE problems are solved using the Residual-Based Attention (RBA) weighting scheme [Anagnostopoulos et al., 2024] within the PIML framework [Raissi et al., 2019], where the training objective is defined as a sum of weighted residuals associated with the PDE differential operator and the boundary/initial condition operators. Specifically, we minimize

$$\mathcal{L}(\boldsymbol{\theta}) = \frac{1}{N_{\text{pde}}} \sum_{i=1}^{N_{\text{pde}}} \left| \alpha_i^{(\text{pde})} r_i^{(\text{pde})}(\boldsymbol{\theta}) \right|^2 + \frac{1}{N_{\text{bc}}} \sum_{i=1}^{N_{\text{bc}}} \left| \alpha_i^{(\text{bc})} r_i^{(\text{bc})}(\boldsymbol{\theta}) \right|^2, \quad (31)$$

where  $\|\cdot\|_2$  denotes the  $L^2$  norm. Here,  $r_i^{(\text{pde})}$  represents the residual of the governing PDE evaluated at the  $i$ -th collocation point, while  $r_i^{(\text{bc})}$  denotes the residual of the boundary or initial condition (both are included in the second summation). The weights  $\alpha_i^{(\xi)}$  ( $\xi \in \{\text{pde}, \text{bc}\}$ ) are initialized to 1 and updated after each training iteration according to

$$\alpha_i^{(\xi), (\text{new})} = \gamma \alpha_i^{(\xi), (\text{old})} + \eta \frac{|r_i^{(\xi)}|}{\max_j \{|r_j^{(\xi)}|\}_{j=1}^{N_\xi}}, \quad (32)$$

with hyperparameters  $\gamma = 0.999$  and  $\eta = 0.01$ . This formulation ensures that collocation points with larger relative residuals are assigned greater importance during optimization<sup>5</sup>.

We minimize the loss function in Eq. (31) using the Adam optimizer with a fixed learning rate of  $10^{-3}$ , operating in full-batch mode. For each PDE, we sample  $N_{\text{pde}} = 2^{12}$  collocation points uniformly from a  $2^6 \times 2^6$  grid, while for boundary and initial conditions we use  $2^6$  collocation points per condition, sampled uniformly along the corresponding axis. The spline basis functions are defined as in the function fitting case (see Appendix C.1).

### C.3 Feynman Dataset

As a third benchmark, we consider the subset of the Feynman dataset used in Section 4.3. The implementation details are identical to those of the function fitting benchmarks in Appendix C.1, with the exception of sampling. In this case, we generate 4,000 random input samples uniformly distributed over the domain  $(-1, 0) \cup (0, 1)$ , explicitly excluding the points  $-1, 0$ , and  $1$  to avoid singularities in certain formulas.

To compute the relative  $L^2$  error between model predictions and reference solutions, we evaluate all trained models on a uniform  $200 \times 200$  grid for two-dimensional functions and a uniform  $30 \times 30 \times 30$  grid for three-dimensional functions. Table 5 lists the indices of the functions included in this benchmark, together with their explicit expressions for reference.

---

<sup>5</sup>Without RBA, the models trained to solve the Allen–Cahn equation would yield highly inaccurate solutions, preventing a meaningful comparison of initialization schemes.

Table 5: Dimensionless formulas from the Feynman dataset used in the benchmark. Each entry shows the dataset index and the corresponding explicit expression.

Index	Formula
I.6.2	$f_1(x_1, x_2) = \exp\left(-\frac{x_1^2}{2x_2^2}\right) \cdot (2\pi x_2^2)^{-1/2}$
I.6.2b	$f_2(x_1, x_2, x_3) = \exp\left(-\frac{(x_1-x_2)^2}{2x_3^2}\right) \cdot (2\pi x_3^2)^{-1/2}$
I.12.11	$f_3(x_1, x_2) = 1 + x_1 \sin(x_2)$
I.13.12	$f_4(x_1, x_2) = x_1(1/x_2 - 1)$
I.16.6	$f_5(x_1, x_2) = (x_1 + x_2)/(1 + x_1 x_2)$
I.18.4	$f_6(x_1, x_2) = (1 + x_1 x_2)/(1 + x_1)$
I.26.2	$f_7(x_1, x_2) = \arcsin(x_1 \sin(x_2))$
I.27.6	$f_8(x_1, x_2) = 1/(1 + x_1 x_2)$
I.29.16	$f_9(x_1, x_2, x_3) = \sqrt{1 + x_1^2 - 2x_1 \cos(x_2 - x_3)}$
I.30.3	$f_{10}(x_1, x_2) = \sin^2(x_1 x_2 / 2) / \sin^2(x_2 / 2)$
I.40.1	$f_{11}(x_1, x_2) = x_1 \exp(-x_2)$
I.50.26	$f_{12}(x_1, x_2) = \cos(x_1) + x_2 \cos^2(x_1)$
II.2.42	$f_{13}(x_1, x_2) = (x_1 - 1)x_2$
II.6.15a	$f_{14}(x_1, x_2, x_3) = \frac{x_3}{4\pi} \sqrt{x_1^2 + x_2^2}$
II.11.7	$f_{15}(x_1, x_2, x_3) = x_1(1 + x_2 \cos(x_3))$
II.11.27	$f_{16}(x_1, x_2) = (x_1 x_2) / (1 - \frac{x_1 x_2}{3})$
II.35.18	$f_{17}(x_1, x_2) = x_1 / (\exp(x_2) + \exp(-x_2))$
II.36.38	$f_{18}(x_1, x_2, x_3) = x_1 + x_2 x_3$
III.10.19	$f_{19}(x_1, x_2) = \sqrt{1 + x_1^2 + x_2^2}$
III.17.37	$f_{20}(x_1, x_2, x_3) = x_2 (1 + x_1 \cos(x_3))$

---

## D Indicative Results for Power-Law Grid-Search

To illustrate the performance landscape of the power-law initialization, we present heatmaps over  $(\alpha, \beta)$  configurations for representative cases. Specifically, Figures 7–10 show results for the function  $f_3(x, y)$  across the four grid sizes, while Figures 11–13 show the corresponding results for the Allen–Cahn PDE. In each heatmap, the horizontal axis corresponds to  $\alpha$  and the vertical axis to  $\beta$ , with rows and columns indicating different network widths and depths, respectively. These visualizations highlight the regions where power-law initialization provides the greatest improvements, and help motivate the choice of  $(\alpha, \beta) = (0.25, 1.75)$  used for the architectures studied in Sections 4.2 and 4.3. Complete heatmaps for all benchmarks are included in the supplementary material (see Reproducibility Statement).

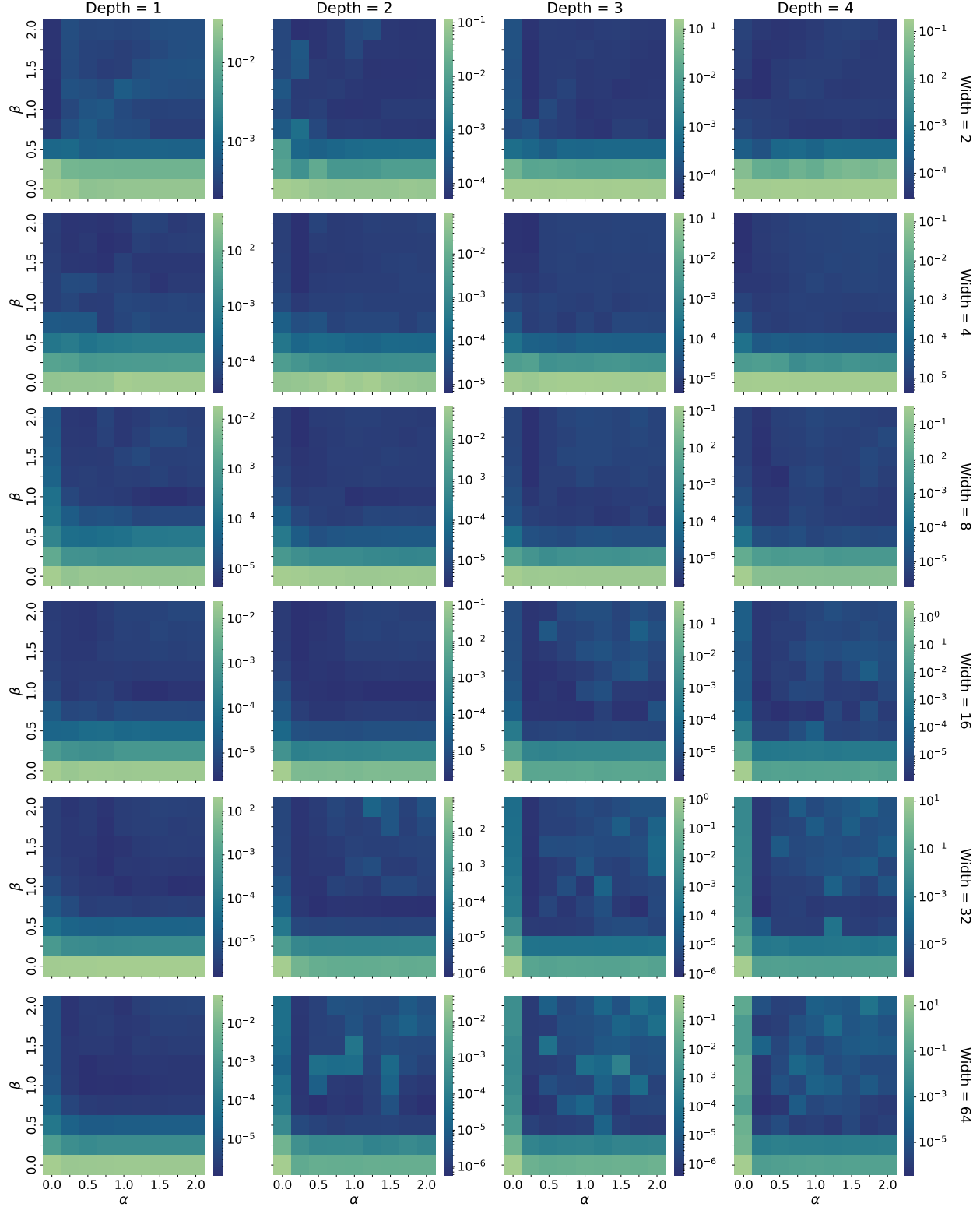


Figure 7: Grid search for the power-law initialization applied to fit function  $f_3(x, y)$  for  $G = 5$ . Each heatmap corresponds to an architecture, with the horizontal and vertical axis representing  $\alpha$  and  $\beta$ , respectively, and color denoting final training loss.

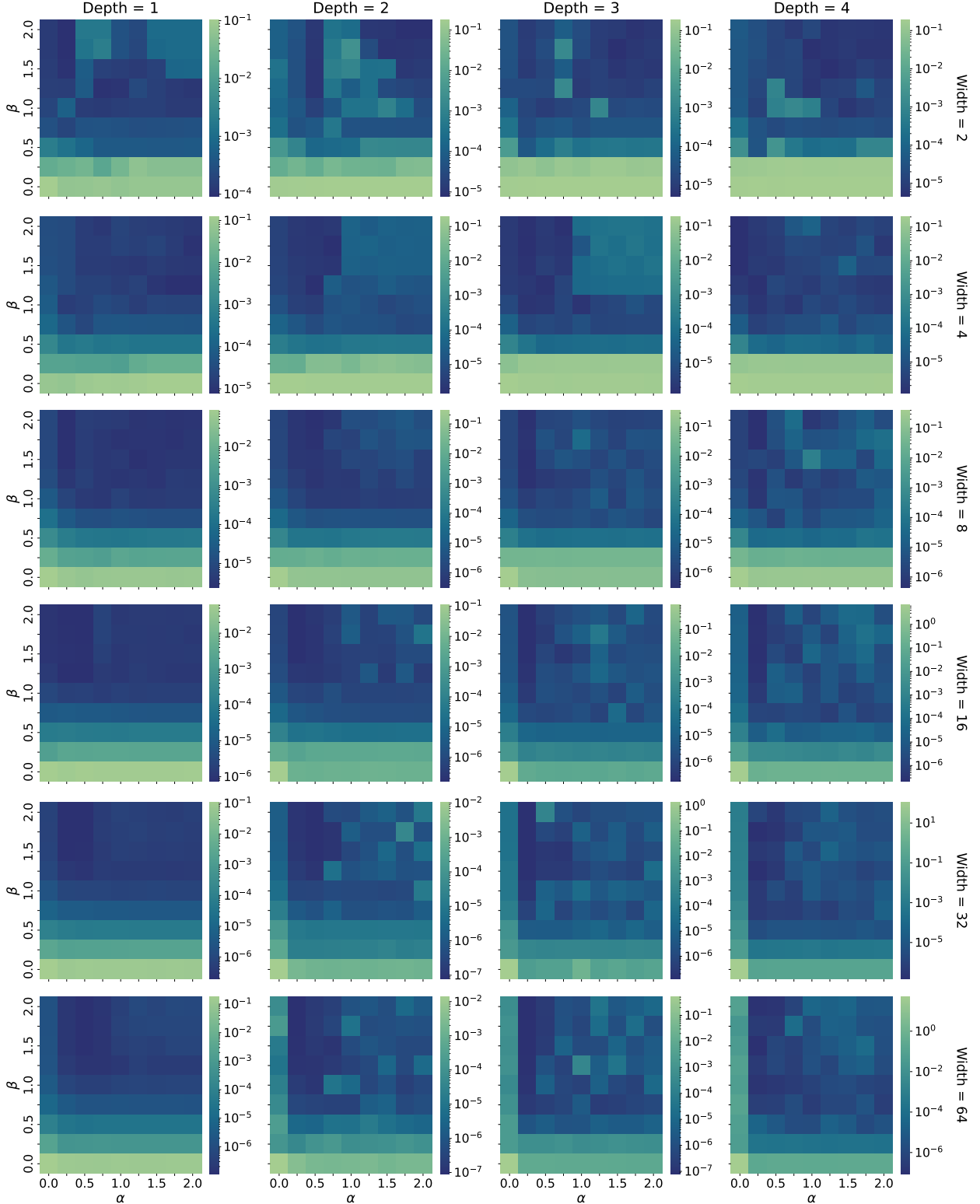


Figure 8: Grid search for the power-law initialization applied to fit function  $f_3(x, y)$  for  $G = 10$ . Each heatmap corresponds to an architecture, with the horizontal and vertical axis representing  $\alpha$  and  $\beta$ , respectively, and color denoting final training loss.

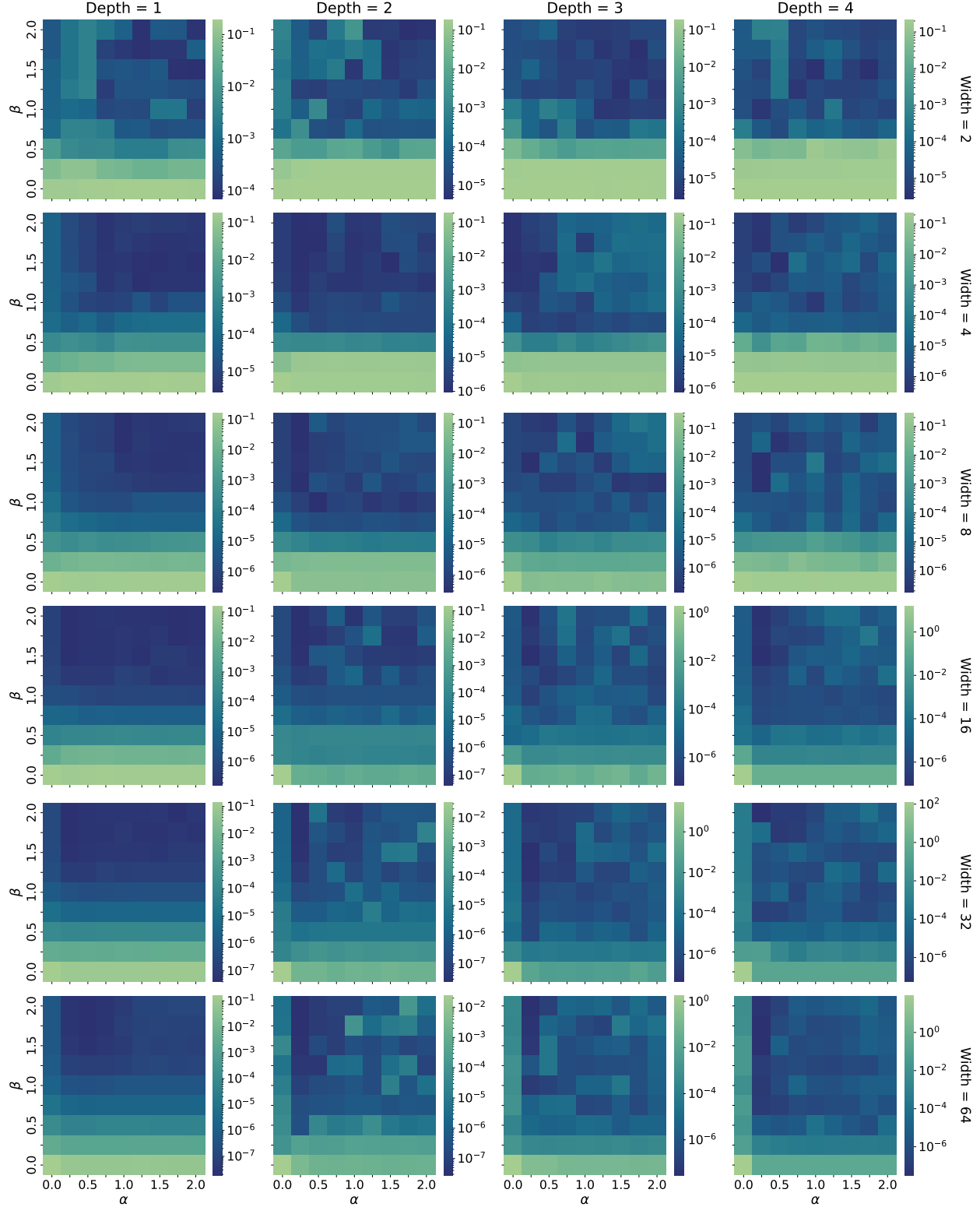


Figure 9: Grid search for the power-law initialization applied to fit function  $f_3(x, y)$  for  $G = 20$ . Each heatmap corresponds to an architecture, with the horizontal and vertical axis representing  $\alpha$  and  $\beta$ , respectively, and color denoting final training loss.

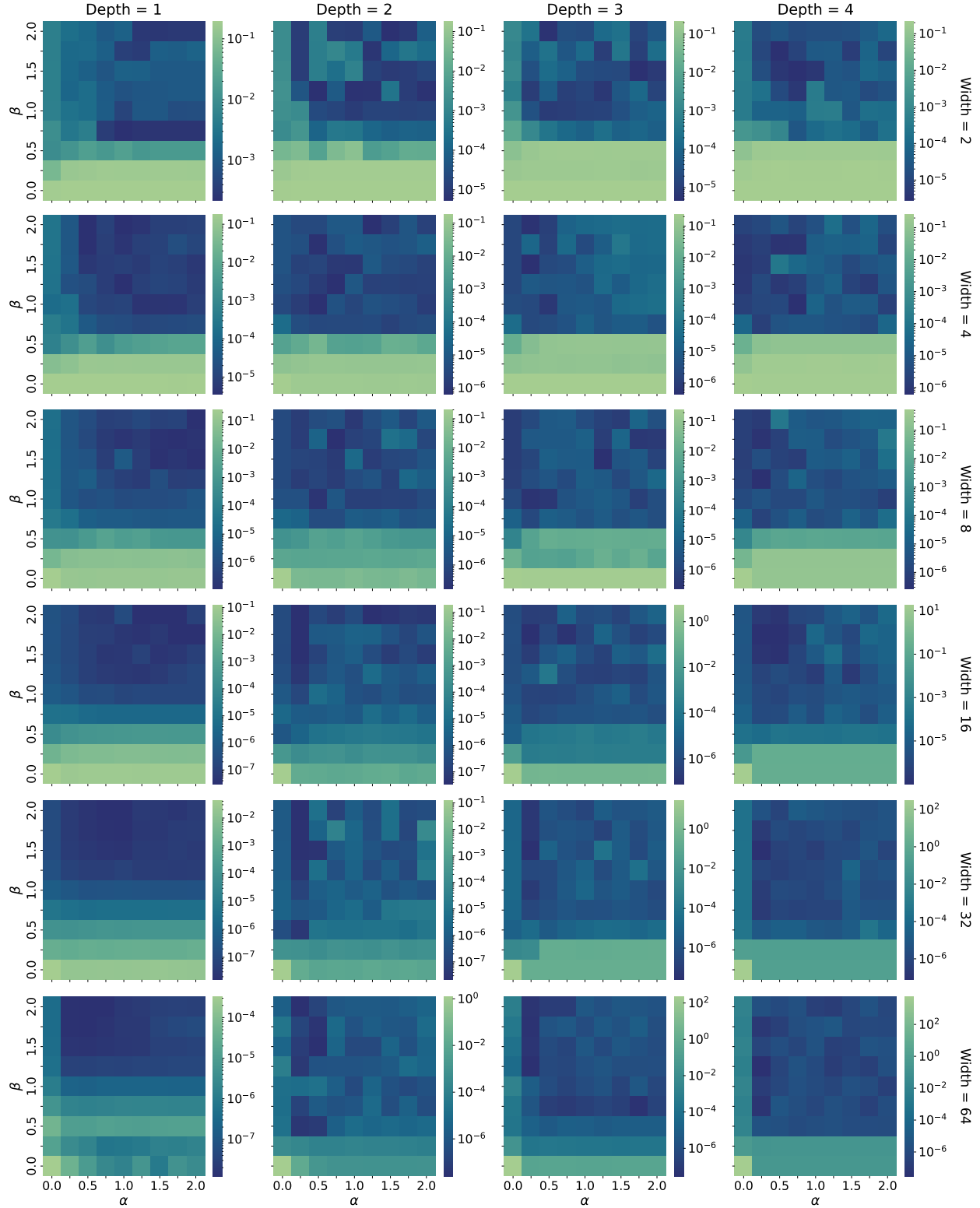


Figure 10: Grid search for the power-law initialization applied to fit function  $f_3(x, y)$  for  $G = 40$ . Each heatmap corresponds to an architecture, with the horizontal and vertical axis representing  $\alpha$  and  $\beta$ , respectively, and color denoting final training loss.

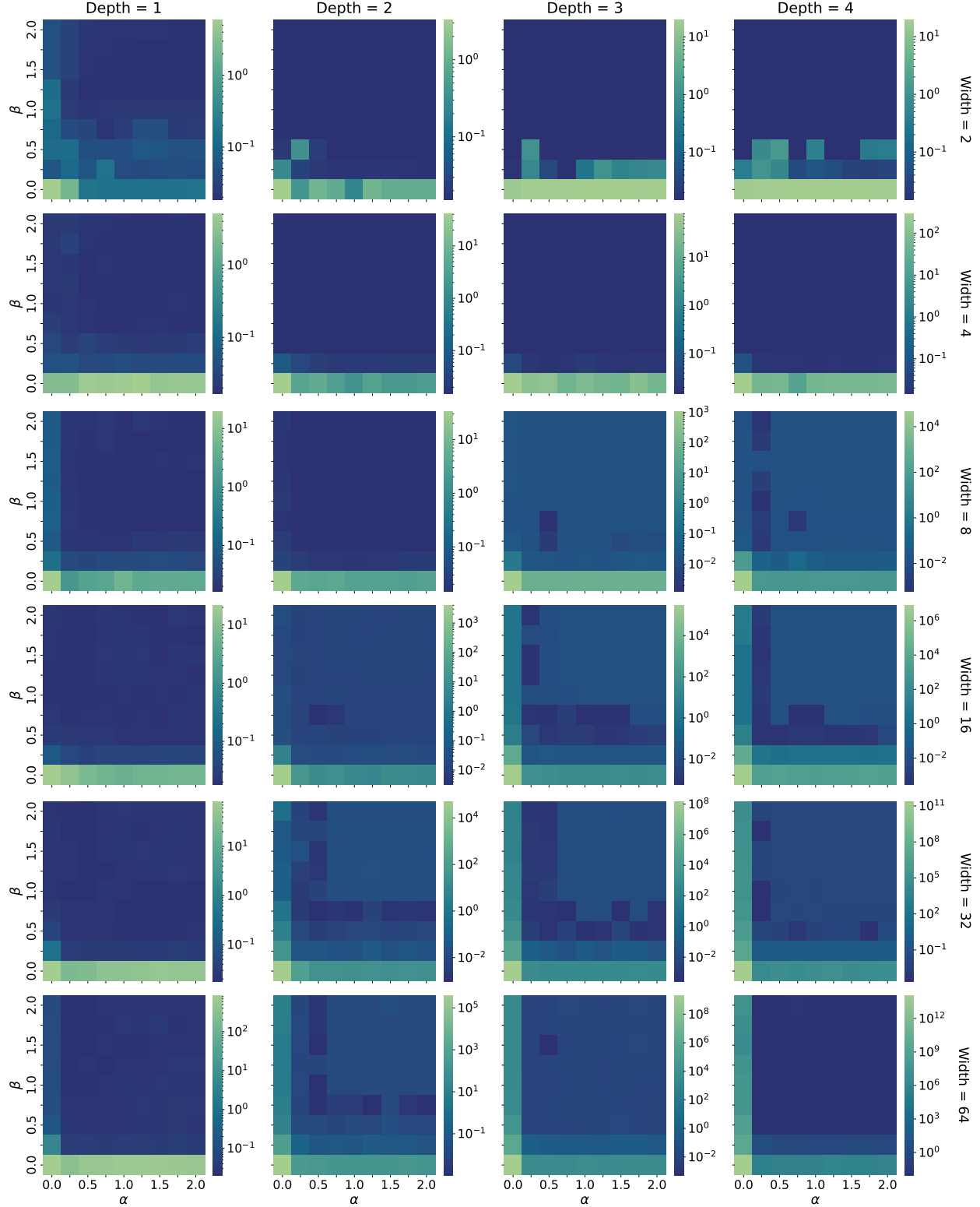


Figure 11: Grid search for the power-law initialization applied for the solution of the Allen–Cahn equation for  $G = 5$ . Each heatmap corresponds to an architecture, with the horizontal and vertical axis representing  $\alpha$  and  $\beta$ , respectively, and color denoting final training loss.

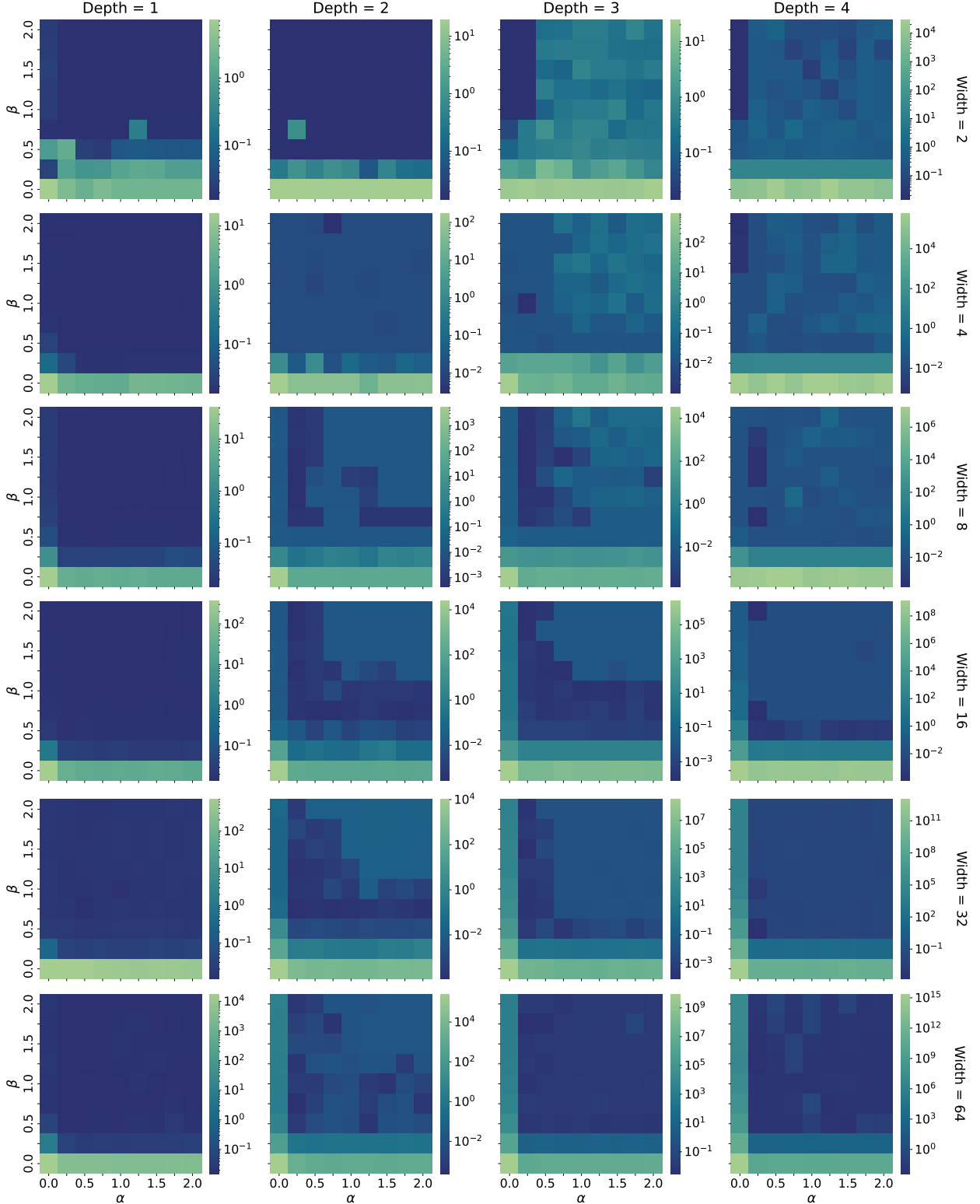


Figure 12: Grid search for the power-law initialization applied for the solution of the Allen–Cahn equation for  $G = 10$ . Each heatmap corresponds to an architecture, with the horizontal and vertical axis representing  $\alpha$  and  $\beta$ , respectively, and color denoting final training loss.

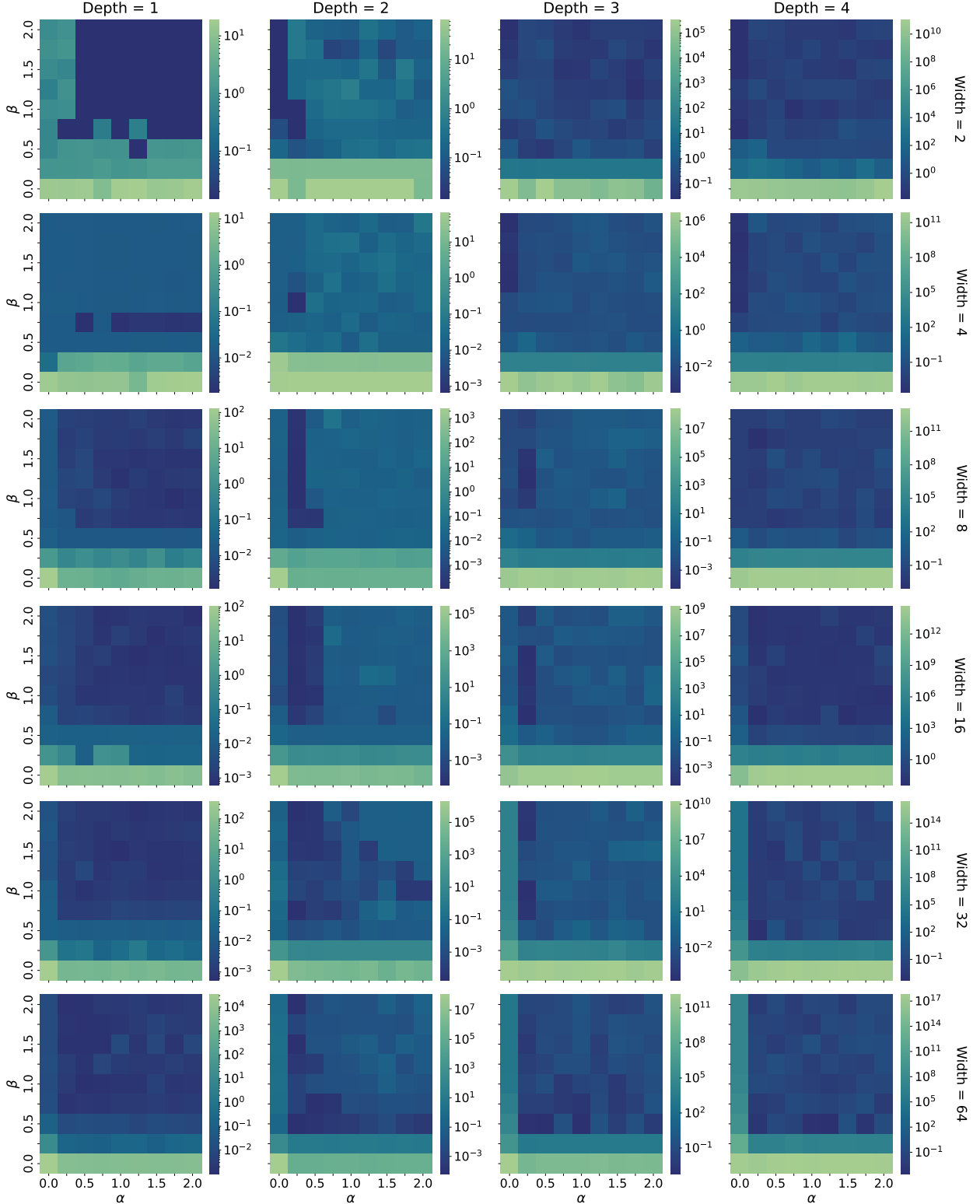


Figure 13: Grid search for the power-law initialization applied for the solution of the Allen–Cahn equation for  $G = 20$ . Each heatmap corresponds to an architecture, with the horizontal and vertical axis representing  $\alpha$  and  $\beta$ , respectively, and color denoting final training loss.

## E Neural Tangent Kernel Analysis

In this work, we use NTK analysis [Jacot et al., 2018] to better understand the effect of initialization schemes on function fitting and PDE benchmarks, both in terms of stability and conditioning.

### E.1 NTK for PIML with RBA Weights

In this subsection, we derive the NTK formalism used in our PDE experiments. Specifically, we extend the standard NTK framework for PIML [Wang et al., 2022] to cover the RBA-weighted loss function of Eq. (31).

We denote the PDE and boundary/initial condition residuals at the  $i$ -th collocation point by  $r_i^{(\text{pde})}$  and  $r_i^{(\text{bc})}$ , respectively, as in Appendix C.2. We may re-weight the loss function of Eq. (31) to follow Wang et al. [2022] and subsequently write it in vector form as

$$\mathcal{L}(\boldsymbol{\theta}) = \frac{1}{2} \|\tilde{\mathbf{r}}^{(\text{pde})}(\boldsymbol{\theta})\|_2^2 + \frac{1}{2} \|\tilde{\mathbf{r}}^{(\text{bc})}(\boldsymbol{\theta})\|_2^2, \quad \tilde{\mathbf{r}}^{(\xi)} = \mathbf{A}^{(\xi)} \mathbf{r}^{(\xi)}, \quad (33)$$

where  $\mathbf{r}^{(\xi)}$  stacks the residuals of type  $\xi \in \{\text{pde}, \text{bc}\}$ ,  $\boldsymbol{\alpha}^{(\xi)} = (\alpha_1^{(\xi)}, \dots, \alpha_{N_\xi}^{(\xi)})^\top$  are the RBA weights and  $\mathbf{A}^{(\xi)} = \text{diag}(\boldsymbol{\alpha}^{(\xi)})$ . Throughout a single gradient step we treat  $\boldsymbol{\alpha}^{(\xi)}$  as constants, as they are updated only between steps by Eq. (32), outside of the gradient descent scheme.

Let  $\mathbf{J}^{(\xi)}(\boldsymbol{\theta}) \in \mathbb{R}^{N_\xi \times P}$  be the Jacobian of the residuals with respect to the parameters, i.e., its  $i$ -th row is  $\mathbf{J}_i^{(\xi)}(\boldsymbol{\theta}) = \partial r_i^{(\xi)}(\boldsymbol{\theta}) / \partial \boldsymbol{\theta}^\top$ . For a parameter update  $\Delta \boldsymbol{\theta} = -\eta \nabla_{\boldsymbol{\theta}} \mathcal{L}(\boldsymbol{\theta})$ , a first-order expansion around  $\boldsymbol{\theta}$  yields,

$$\Delta \tilde{\mathbf{r}}^{(\xi)}(\boldsymbol{\theta}) = \mathbf{A}^{(\xi)} \Delta \mathbf{r}^{(\xi)}(\boldsymbol{\theta}) \approx \mathbf{A}^{(\xi)} \mathbf{J}^{(\xi)}(\boldsymbol{\theta}) \Delta \boldsymbol{\theta}. \quad (34)$$

Using Eq. (33) and the chain rule, the full-batch gradient is

$$\nabla_{\boldsymbol{\theta}} \mathcal{L}(\boldsymbol{\theta}) = \sum_{i=1}^{N_{\text{pde}}} \tilde{r}_i^{(\text{pde})}(\boldsymbol{\theta}) \nabla_{\boldsymbol{\theta}} \tilde{r}_i^{(\text{pde})}(\boldsymbol{\theta}) + \sum_{i=1}^{N_{\text{bc}}} \tilde{r}_i^{(\text{bc})}(\boldsymbol{\theta}) \nabla_{\boldsymbol{\theta}} \tilde{r}_i^{(\text{bc})}(\boldsymbol{\theta}). \quad (35)$$

Since  $\tilde{r}_i^{(\xi)} = \alpha_i^{(\xi)} r_i^{(\xi)}$  and  $\boldsymbol{\alpha}^{(\xi)}$  is held fixed within the step,

$$\nabla_{\boldsymbol{\theta}} \tilde{r}_i^{(\xi)}(\boldsymbol{\theta}) = \alpha_i^{(\xi)} \nabla_{\boldsymbol{\theta}} r_i^{(\xi)}(\boldsymbol{\theta}) = \alpha_i^{(\xi)} (\mathbf{J}_i^{(\xi)}(\boldsymbol{\theta}))^\top. \quad (36)$$

Substituting  $\Delta \boldsymbol{\theta} = -\eta \nabla_{\boldsymbol{\theta}} \mathcal{L}(\boldsymbol{\theta})$  into Eq. (34) and grouping terms gives the linear dynamics

$$\begin{aligned} \Delta \tilde{\mathbf{r}}^{(\xi)}(\boldsymbol{\theta}) &\approx -\eta \left[ \underbrace{(\mathbf{A}^{(\xi)} \mathbf{J}^{(\xi)}(\boldsymbol{\theta})) (\mathbf{A}^{(\text{pde})} \mathbf{J}^{(\text{pde})}(\boldsymbol{\theta}))^\top}_{\tilde{\mathbf{K}}^{(\xi, \text{pde})}} \tilde{\mathbf{r}}^{(\text{pde})}(\boldsymbol{\theta}) \right. \\ &\quad \left. + \underbrace{(\mathbf{A}^{(\xi)} \mathbf{J}^{(\xi)}(\boldsymbol{\theta})) (\mathbf{A}^{(\text{bc})} \mathbf{J}^{(\text{bc})}(\boldsymbol{\theta}))^\top}_{\tilde{\mathbf{K}}^{(\xi, \text{bc})}} \tilde{\mathbf{r}}^{(\text{bc})}(\boldsymbol{\theta}) \right]. \end{aligned} \quad (37)$$

As mentioned in the main text, Eq. (37) shows that the weighted residual vectors  $\tilde{\mathbf{r}}^{(\xi)}$  evolve under a weighted NTK with blocks

$$\tilde{\mathbf{K}}^{(\xi, \zeta)} = (\mathbf{A}^{(\xi)} \mathbf{J}^{(\xi)}) (\mathbf{A}^{(\zeta)} \mathbf{J}^{(\zeta)})^\top, \quad \xi, \zeta \in \{\text{pde}, \text{bc}\}. \quad (38)$$

## E.2 Additional NTK Spectra

For completeness, we report additional NTK spectra not included in the main text. Figures 14–17 show the results for the remaining function fitting benchmarks ( $f_1, f_2, f_4, f_5$ ), while Figures 18, 19 correspond to the Burgers' and Helmholtz PDEs. All results are obtained using the “large” architecture ( $G = 20$ , three hidden layers with 32 neurons each), consistent with the setting analyzed in Section 4.2.



Figure 14: Eigenvalue spectra of the NTK matrix at initialization (solid blue), intermediate iterations (dashed teal), and final iteration (dashed green) for function fitting benchmark  $f_1(x, y)$  under different initialization strategies.

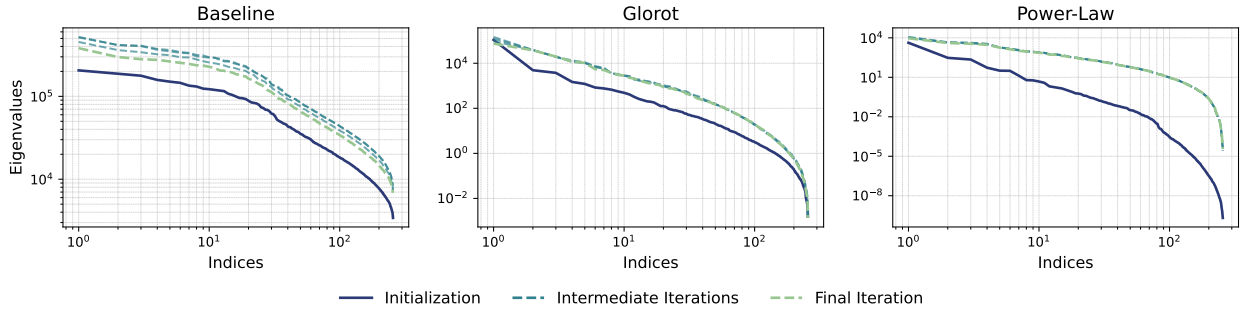


Figure 15: Eigenvalue spectra of the NTK matrix at initialization (solid blue), intermediate iterations (dashed teal), and final iteration (dashed green) for function fitting benchmark  $f_2(x, y)$  under different initialization strategies.



Figure 16: Eigenvalue spectra of the NTK matrix at initialization (solid blue), intermediate iterations (dashed teal), and final iteration (dashed green) for function fitting benchmark  $f_4(x, y)$  under different initialization strategies.

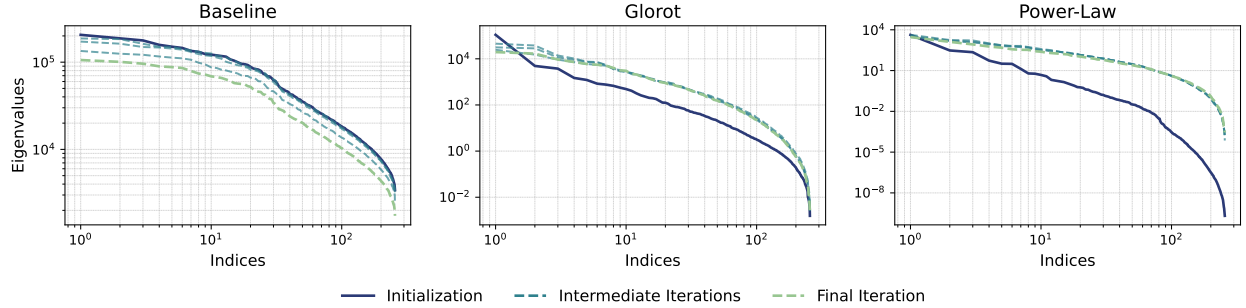


Figure 17: Eigenvalue spectra of the NTK matrix at initialization (solid blue), intermediate iterations (dashed teal), and final iteration (dashed green) for function fitting benchmark  $f_5(x, y)$  under different initialization strategies.

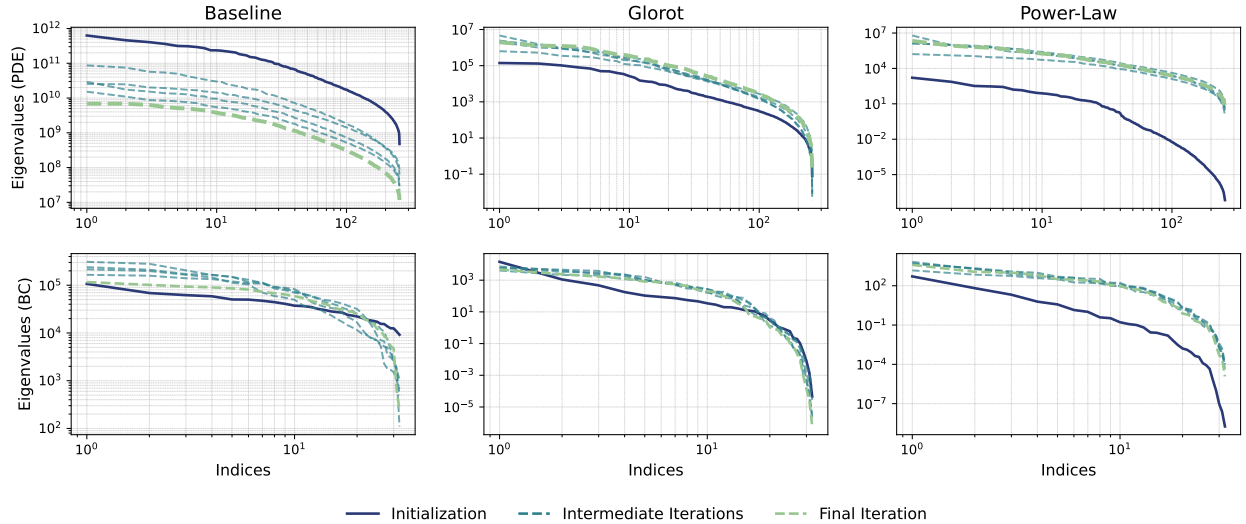


Figure 18: NTK eigenvalue spectra for the Burgers' PDE benchmark under baseline, Glorot, and power-law initializations. Top row: spectra corresponding to the PDE residual term. Bottom row: spectra for the boundary/initial condition terms. Solid lines show the initialization, dashed lines show intermediate iterations, and dotted lines show the final iteration.

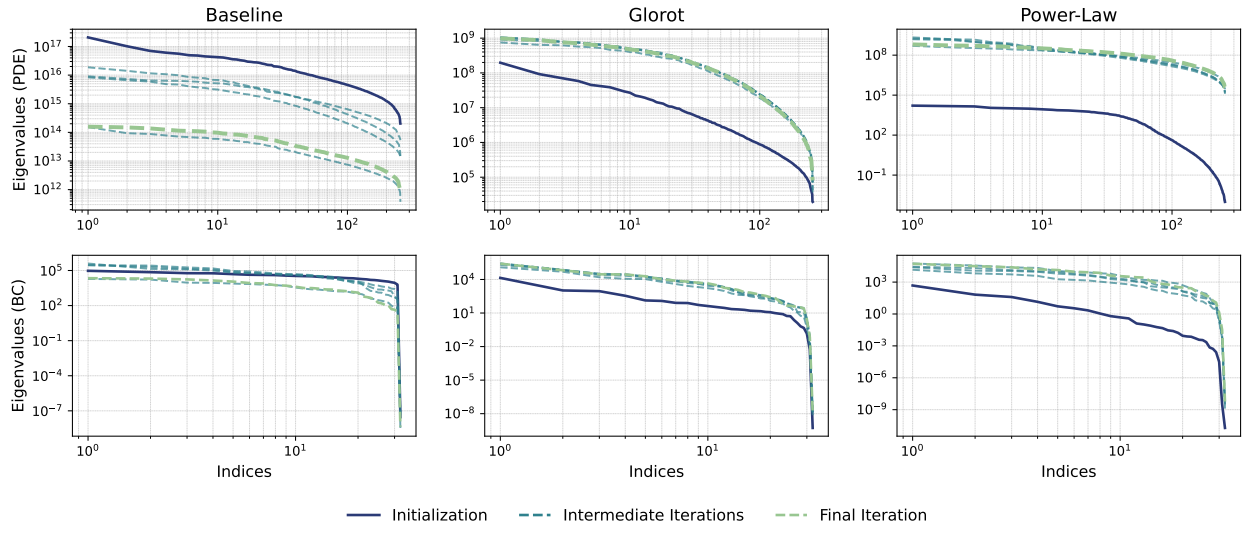


Figure 19: NTK eigenvalue spectra for the Helmholtz PDE benchmark under baseline, Glorot, and power-law initializations. Top row: spectra corresponding to the PDE residual term. Bottom row: spectra for the boundary/initial condition terms. Solid lines show the initialization, dashed lines show intermediate iterations, and dotted lines show the final iteration.